BMC Medicine

RESEARCH

Open Access

FLASH radiotherapy preserves systemic and tissue homeostasis while maintaining antitumor efficacy

Giulia Furini[1†], Eduarda Mota da Silva[1†], Alice Usai[1], Gaia Scabia[1], Claudia Kusmic[1], Francesco Faita[1], Andrea Cavalieri[2,3], Mariagrazia Celentano[2], Mario Costa[4], Filippo Rossi[1], Giulia Asero[1], Roberta Di Pietro[5], Emanuela Guerra[5], Stefano Lattanzio[5], Tonia Luca[6], Sergio Castorina[6], Roberto Cusano[7], Riccardo Berutti[7], Jessica Milia[7], Simone Capaccioli[2,3,8], Alessandra Gonnelli[2,9], Noemi Giannini[2,9], Fabiola Paiar[2,10], Saverio Cinti[11], Fabio Di Martino[2,12] and Margherita Maffei[1,13*]

Abstract

Background Conventional radiotherapy (CONV-RT) is widely used for cancer treatment, but its efficacy is limited by toxicity to surrounding healthy tissues. Ultra-high dose rate radiotherapy (FLASH-RT) has emerged as a promising approach, maintaining tumor control while sparing normal tissues. Melanoma is highly radioresistant, and deep-seated lesions expose skin and muscle to radiation, causing long-term fibrosis, stiffness, and loss of elasticity. The aim of this study is to compare the efficacy and collateral effects of CONV-RT and FLASH-RT, using melanoma as a benchmark for tumor response and skin–muscle as a model for normal tissue toxicity, and to investigate the underlying molecular and systemic mechanisms.

Methods A novel linear accelerator (LINAC) delivering low-energy electrons at ultra-high dose rate via a triode gun with precise tissue targeting and dose delivery was used. CONV-RT and FLASH-RT were administered to a syngeneic melanoma mouse model. Tumor growth, skin and muscle integrity, transcriptional changes, and systemic homeostasis were analyzed in tumor-bearing and naïve mice.

Results Both modalities achieved comparable tumor suppression. CONV-RT induced persistent skin damage, dermal fibrosis, muscle dysfunction, and systemic inflammatory–metabolic alterations, whereas FLASH-RT largely preserved tissue architecture and systemic balance. Bulk RNA sequencing revealed minimal transcriptional disruption after FLASH-RT, while CONV-RT triggered thousands of differentially expressed genes, including pathways related to fibrosis, inflammation, cell death in skin, and muscle remodeling, function, and the unfolded protein response. Histological and ultrastructural analyses confirmed reduced immune infiltration and preserved tissue structure following FLASH-RT.

Conclusions FLASH-RT provides effective tumor control while largely preserving normal tissues. CONV-RT and FLASH-RT elicit substantially different biological responses, suggesting the involvement of upstream modulators that vary depending on the dose rate.

[†]Giulia Furini and Eduarda Mota Da Silva contributed equally to this work.

*Correspondence:
Margherita Maffei
margherita.maffei@cnr.it
Full list of author information is available at the end of the article

Keywords Ultra-high-dose-rate radiotherapy, Melanoma, Radiation injuries, Long-term effects, Cachexia

Graphical Abstract

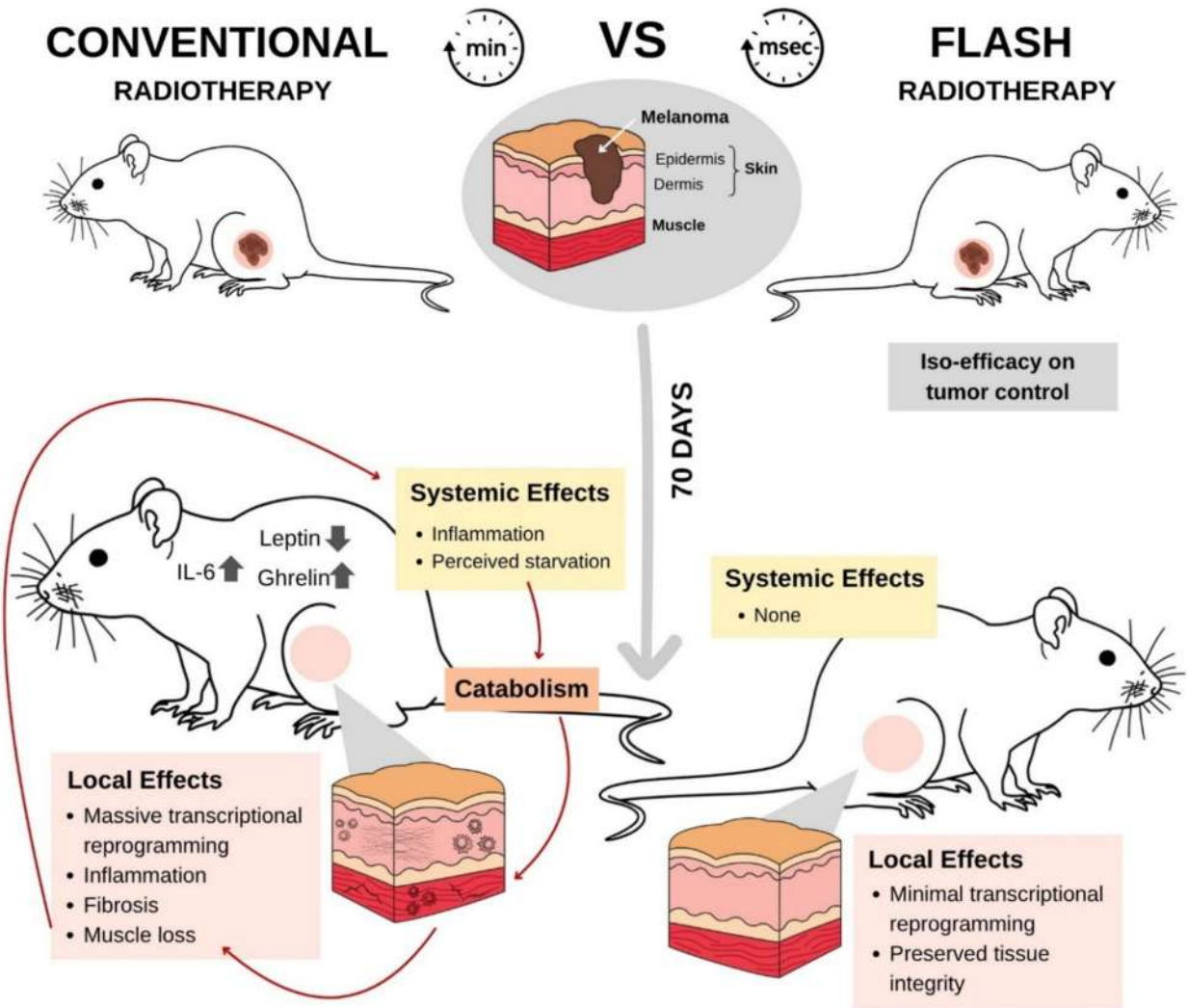

Background

Radiotherapy (RT) represents one of the main pillars of modern oncology, with approximately 50–60% of patients receiving RT during the course of their disease and contributing to definitive cure in nearly 40% of cases. Despite remarkable technological advancements in dose delivery and image guidance, one of the most critical challenges remains its unavoidable toxicity to surrounding normal tissues. The skin in particular represents both a barrier and a vulnerable target: it is exposed during irradiation of superficial as well as deep-seated tumors, and radiation-induced skin damage is among the most frequent and clinically relevant adverse effects. Indeed, skin toxicity is reported in nearly 90% of patients undergoing RT, ranging from erythema and desquamation to late effects such as atrophy, fibrosis, and necrosis, with fibrosis-related dysfunction recognized as the most severe long-term complication [1].

Melanoma exemplifies the dual challenge of tumor radio-resistance and treatment-associated toxicity. It ranks as the 17th most common cancer worldwide,

with approximately 331,700 new cases in 2022, and its incidence continues to rise [2]. Despite significant progress achieved through immune checkpoint inhibitors and targeted therapies, the prognosis for advanced melanoma remains poor, with a global 5-year survival rate of ~ 50% [3]. RT, often used as part of multimodal regimens, provides local control in specific clinical scenarios; however, the intrinsic radio-resistance of melanoma, coupled with frequent relapses, underscores the urgent need for novel and more effective RT approaches [4].

In recent years, ultra-high-dose-rate (UHDR) radiotherapy (FLASH-RT) has emerged as a promising strategy to mitigate toxicity without compromising tumor control. FLASH-RT delivers radiation at dose rates several orders of magnitude higher than conventional RT (CONV-RT), typically ≥ 40 Gy/s compared to ~ 0.1–0.5 Gy/s. Strikingly, multiple preclinical studies have reported that FLASH-RT spares normal tissues across various organs — including brain, lung, intestine, and skin — while maintaining iso-effective tumor control. This so-called "FLASH effect" has been demonstrated in mice [5–9] as well as in larger animals such as minipigs and cats [10], suggesting broad translational potential. Importantly, the magnitude of this protective effect appears dose-dependent, with higher total doses often producing more pronounced tissue sparing [5, 10].

FLASH-RT has been tested across various radiation sources: photon, protons, and electrons. Limited studies are available with the use of photons due to the lack of devices capable of delivering X-ray beams at high dose rates [11]; as for protons, while high-current delivery has been demonstrated in preclinical settings [7, 12–14], translation to routine clinical use demands further development in planning systems, safety protocols, and hardware modifications [15]. Low-energy electrons have been utilized most commonly to demonstrate the FLASH effect thus far [16], as they achieve a reproducible and readily available dose control, although their limited depth penetration (few cm) is an obstacle for its full implementation into the clinic [11] and sources able to release very high energy electrons, not yet available, are required to reach deep seated tumors.

Despite these promising observations, the mechanisms underlying the FLASH effect remain poorly understood. Hypotheses include oxygen depletion during ultra-fast delivery, altered redox signaling, and differential activation of DNA damage responses [17, 18]. However, definitive mechanistic evidence is still lacking.

FLASH-RT has rapidly gained attention due to its normal tissue–sparing effects; however, data on tumor response remain limited. In particular, the frequently reported preservation of tumor control compared to conventional radiotherapy (CONV-RT) is based on a small number of well-planned in vivo studies, involving only a few tumor types and specific mouse models. Consequently, the generalizability of this assumption across different tumor entities and biological contexts remains an open question [19]. While tumor control by FLASH-RT has been shown to be comparable to CONV-RT in models of sarcoma and lung carcinoma [14, 16], data on melanoma — a relatively rare but clinically significant cancer — remain scarce. Given its notorious radio resistance, melanoma represents a particularly stringent benchmark for assessing the therapeutic relevance of FLASH-RT [20]. Although RT is not the standard primary treatment for melanoma, it is routinely employed in several well-established clinical settings, including adjuvant treatment of regional nodal disease, stereotactic irradiation of brain and extracranial metastases, and palliative treatment of symptomatic lesions. Clinical trials employing FLASH-RT are currently ongoing for melanomas [21, 22]. These indications motivated the selection of melanoma as clinically relevant. At the same time, the superficial localization of many melanoma lesions renders skin toxicity a clinically meaningful endpoint.

Another underexplored dimension is the relationship between local irradiation and systemic responses. Radiation not only damages tissues directly within the beam path but also triggers complex systemic effects, including metabolic, endocrine, and immune alterations [23]. These broader responses may influence both treatment tolerance and efficacy. Yet, few studies have examined how FLASH versus CONV irradiation differentially impact systemic physiology beyond the irradiated tissue. For example, changes in energy balance regulating hormones such as leptin and ghrelin, or transcriptional remodeling in non-tumor tissues, may reveal previously unrecognized dimensions of the FLASH effect.

To address these gaps, we compared electron FLASH and CONV-RT in a syngeneic melanoma model, with a specific focus on late normal tissue responses, which remain relatively underreported in the FLASH literature, especially with respect to transcriptomic changes, as such analyses are typically performed under acute, short-term conditions and may therefore overlook effects that emerge at later time points [14]. In addition to tumor growth control and local effects, we assessed long-term systemic effects of irradiation, including body weight dynamics, metabolic and endocrine parameters, and gene expression programs in healthy irradiated tissues.

For this purpose, we exploited a clinical linear accelerator (linac) modified to deliver both CONV and electron FLASH beams within the same platform [24], ensuring maximal comparability. This approach enabled us to characterize, in a translationally relevant

setting, how different dose-rate modalities shape not only local toxicity but also systemic responses in irradiated mice.

Methods

Experimental design

This study aims to investigate the effects of electron CONV-RT versus UHDR FLASH-RT in both a syngeneic melanoma model and a naïve model, evaluating its impact on tumor progression and healthy tissues potentially affected by the therapy, as well as its systemic effects. RT was delivered by a novel linac specifically designed to enable reproducible and finely tunable control of electron beam parameters. The energy of the delivered dose remains relatively uniform within the first 1–2 cm from the surface, enabling us to investigate the biological effects of both CONV- and FLASH-RT not only in the skin but also in the underlying muscle tissue.

C57BL/6J mice were randomly assigned to either the melanoma ($n=4$–8 mice per group) or the naïve model ($n=5$–8 mice per group) (Figs. 1a and 2a). In the former, mice were inoculated with B16-F10 cells in the left hindlimb and received irradiation (19 Gy or 33.3 Gy) 5 days later. In the naïve model, mice received 33.3 Gy irradiation to the same limb 1–2 days after being housed. For consistency throughout the manuscript, "Day 0" is defined as the day of tumor inoculation in the melanoma model and the day of RT in the naïve model. Melanoma mice were monitored for up to 35 days, while naïve mice were sacrificed 70 days post-RT to assess mid- and long-term effects. Animals reaching humane endpoints, due to either tumor burden or general health deterioration, were euthanized earlier.

Survival, physical parameters, glucose regulation, and systemic levels of inflammatory markers and metabolic hormones were evaluated in both models longitudinally from day 0 to sacrifice. Ultrasound analysis was performed to evaluate tumor progression in the melanoma model. In the naïve model, we investigated the impact of CONV versus FLASH-RT on skin and muscle tissues exposed to RT by high-throughput gene expression profiling, histological analysis using both optical and electron microscopy. In addition, we scored skin toxicity using a scale devised for this study. Data analysis was performed blindly. Detailed information on the number of mice specifically used for each experimental parameter is provided in Additional file 3: Table S1.

Animals

Male C57BL/6J mice (6–7 weeks old) were purchased from Charles River Laboratories Italia SRL. Following a 2-week acclimatization period in the animal facility, animals were housed individually (melanoma tumor model) or in groups of 3–4 per cage (naïve group). Food and water were available ad libitum. Body weight (BW) was monitored at baseline and then weekly throughout the experimental period. Food and water intake were recorded twice per week. At the time of sacrifice, skin and muscle tissues from the irradiated area were dissected and either snap-frozen in liquid nitrogen for RNA and/or protein extraction or formalin-fixed for histological analysis.

All procedures were carried out in accordance with the Helsinki guidelines for animal experimentation and

(See figure on next page.)

Fig. 1 Comparative effects of FLASH- and CONV-RT on tumor progression, survival and vital parameters. **a** Experimental design/timeline describing the experiments performed in tumor bearing mice, see Methods for further details. **b** Mice irradiation setup: on the left, mice positioned on a 3D-printed support. On the right, precise placement of the applicator onto the mouse thigh. **c** Kaplan–Meier survival curves of melanoma-bearing mice not irradiated (CNT) or irradiated with FLASH- or CONV-RT (19 or 33.3 Gy). Sample size: $n=8$ (CNT), $n=6$ (FLASH 19 Gy), $n=5$ (CONV 19 Gy), $n=4$ (FLASH and CONV 33.3 Gy). **d** Representative ultrasound images of tumors treated with 33.3 Gy. **e** Mean tumor volume change over time in mice treated with FLASH or CONV irradiation (19 or 33.3 Gy). Tumor volume was normalized to the baseline measurement obtained immediately prior to RT. Data are presented as mean ± SEM of the $\log_2$-transformed tumor volume–to–baseline ratio, with individual mouse values shown. Sample sizes: $n=7$ (CNT), $n=6$ (FLASH 19 Gy), $n=5$ (CONV 19 Gy), $n=4$ (FLASH and CONV 33.3 Gy). In the 19 Gy CONV-RT and FLASH-RT groups, the reduced number of displayed data points at time points ≥ 21 days reflects the euthanasia of animals due to excessive tumor burden. In contrast, in the 33.3 Gy CONV-RT and FLASH-RT groups, the reduced number of displayed data points at time points ≥ 21 days reflects the occurrence of one complete remission in each group (tumor volume = 0), which could not be displayed due to the logarithmic ($\log_2$) scale of the *y*-axis. Statistical analysis: matched mixed-effects model (REML) followed by Tukey's multiple comparison test. Fixed effects: 19 Gy — Time, $F(1.587, 6.879)=1.67$, $p=0.25$; RT, $F(2, 16)=10.90$, $p=0.001$. 33.3 Gy — Time, $F(1.039, 7.276)=0.11$, $p=0.75$; RT, $F(2, 12)=7.27$, $p=0.0086$. **f** Representative macroscopic images of tumor-bearing legs from two animals treated with 35 Gy FLASH or CONV-RT, taken at baseline and at days 21, 28, and 35 post-RT. **g** Vital parameters in CNT and irradiated mice (33.3 Gy): body weight change, expressed as the relative difference from baseline, food and water intake. Data are presented as mean ± SEM. Sample sizes: $n=5$ (CNT) and $n=4$ (FLASH and CONV). Statistical analysis: matched mixed-effects model (REML) followed by Tukey's multiple comparison test. Fixed effects: Body-weight change — Time, $F(2.567, 21.18)=5.02$, $p=0.0113$; RT, $F(2, 10)=1.60$, $p=0.25$. Food intake — Time, $F(2.317, 19.92)=9.39$, $p=0.0009$; RT, $F(2, 10)=0.59$, $p=0.57$. Water intake — Time, $F(2.685, 22.01)=33.58$, $p<0.0001$; RT, $F(2, 10)=10.49$, $p=0.0035$. Comparisons between groups: * = CNT vs CONV, § = CNT vs FLASH; comparisons between different timepoints in CNT as indicated by brackets

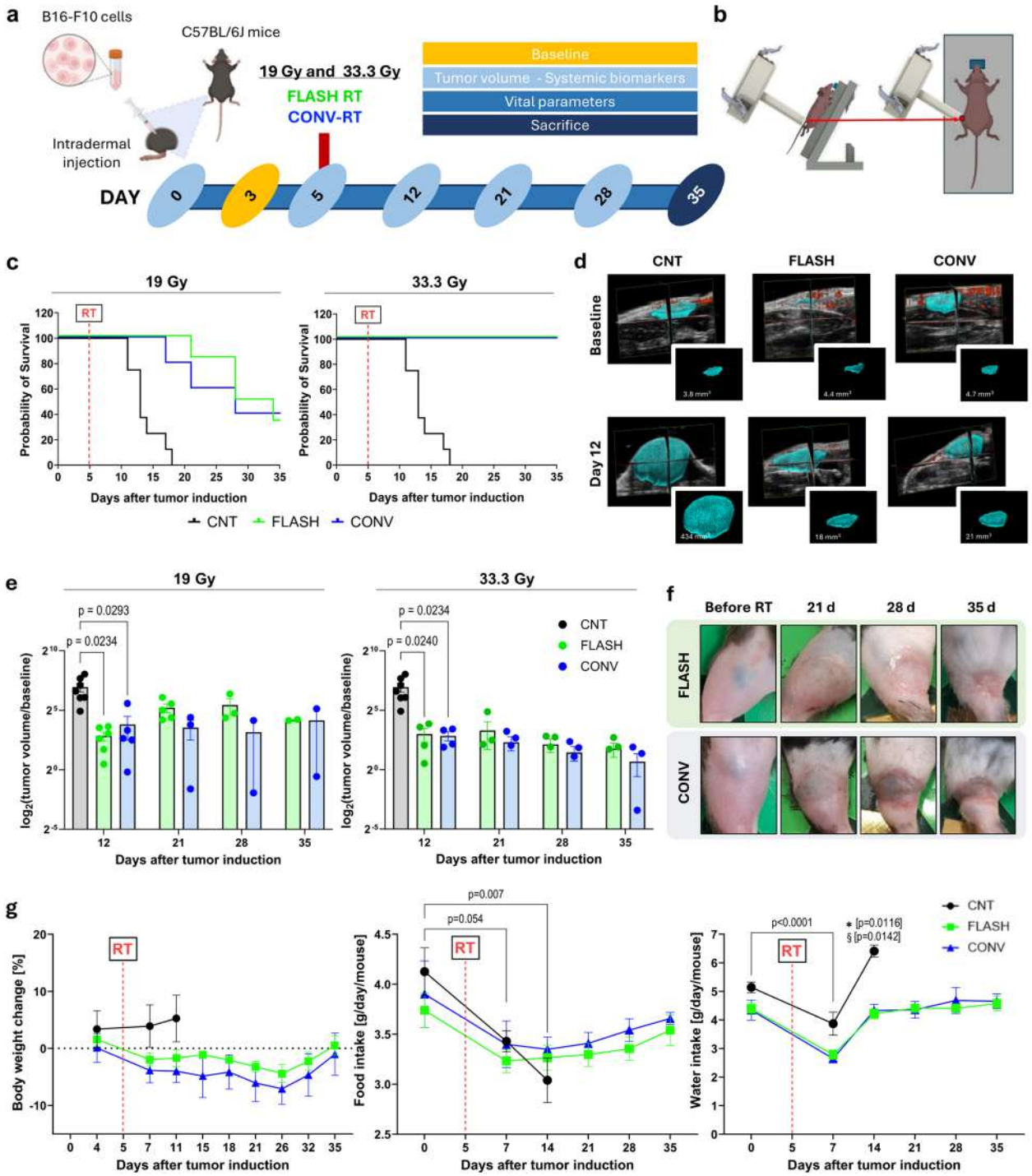

Fig. 1 (See legend on previous page.)

approved under Authorized Protocol 1006/2023-PR, dated November 28, 2023.

Irradiation study design

All the irradiations were performed at the Centro Pisano FLASH Radiotherapy (CPFR) using the ElectronFlash linear accelerator [24], which delivers electron beams of 7 or 9 MeV with the possibility of modifying the average

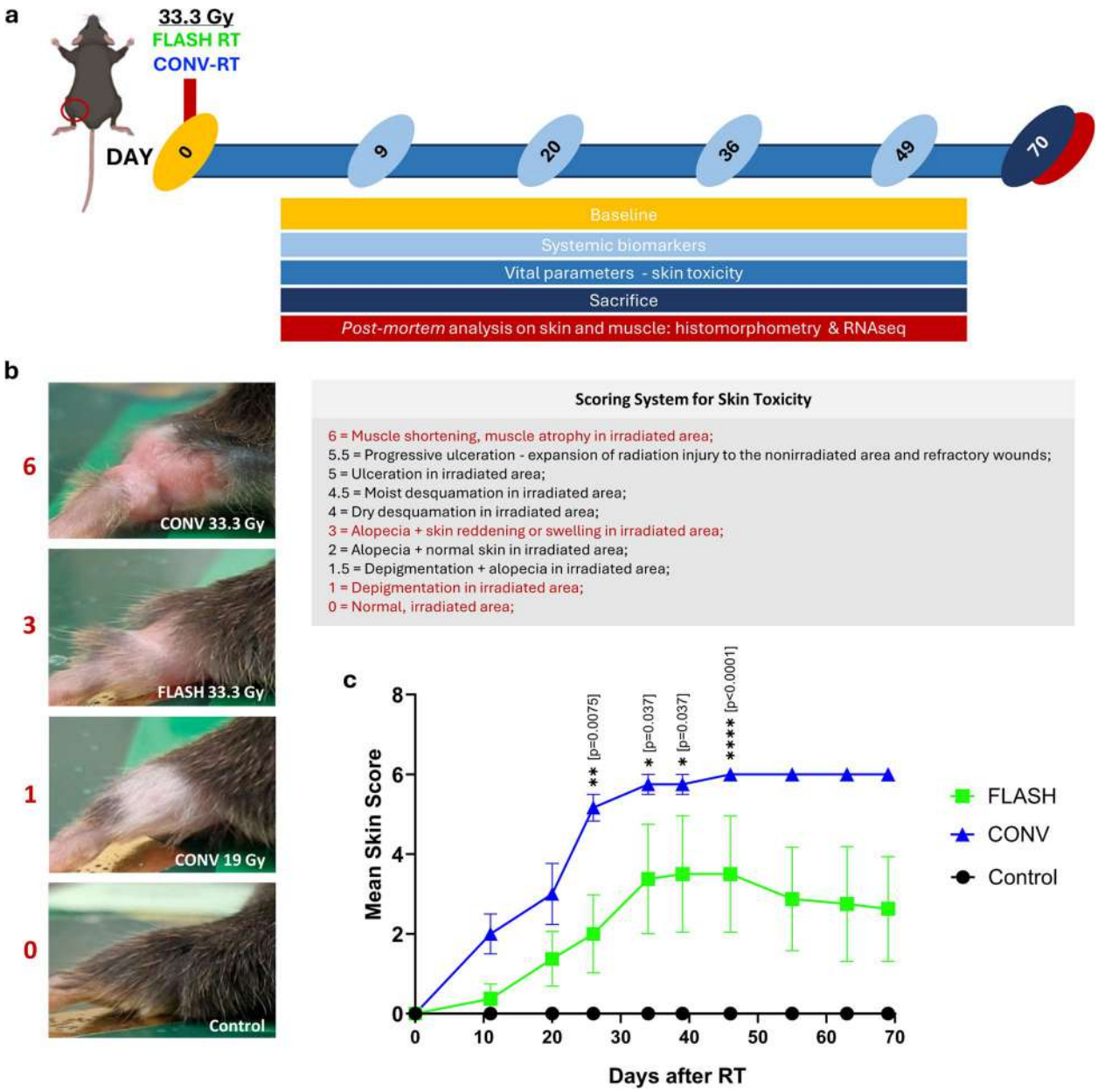

Fig. 2 Skin toxicity in naïve mice. **a** Experimental design/timeline describing the experiments performed in naïve mice, see Methods for further details. Mice were treated with 33.3 Gy CONV- or FLASH-RT to the left hindlimb; matched non-irradiated mice served as CNT. **b** Skin toxicity scores were assessed in naïve mice. Skin reactions were evaluated longitudinally using a semi-quantitative scoring system (0–6 scale) developed within the present project, with higher scores indicating increased severity of skin damage (see representative images in the left panel). Scores were independently and blindly assigned by three researchers using the defined 0–6 scale and averaged to obtain a final score for each mouse. **c** Longitudinal quantification of skin toxicity scores. Data are presented as mean ± SEM. Sample sizes: $n = 4$ (CNT and FLASH) and $n = 3$ (CONV). Statistical analysis: matched mixed-effects model (REML) followed by Tukey's multiple comparison test. Fixed effects: Time, $F(1.607, 13.50) = 5.960$, $p = 0.0181$; RT, $F(2, 8) = 9.318$, $p = 0.0081$. Comparisons between groups: * = CNT vs CONV

dose-rate (ADR) and dose per pulse (DPP) by varying the e-beam current and the pulse repetition frequency (PRF). This allows to switch the irradiation characteristics from the conventional condition (CONV) to the "FLASH" condition, while keeping the experimental setup. All set parameters are summarized in Table 1.

All irradiations were performed on anesthetized mice (ketamine 100 mg/kg/xylazine 10 mg/kg, i.p.) using a collimator with 10 mm diameter centered on the animal's

Table 1 Radiotherapy experimental parameters: relevant parameters used in each irradiation condition

	Total dose [Gy]	Number of pulses	DPP [Gy]	Pulse duration [μs]	PRF [Hz]	ADR [Gy/s]
FLASH-RT	19.0	4	4.75	4	145	940
	33.3	7	4.75	4	170	940
CONV-RT	19.0	103	0.19	4	1	0.18
	33.3	180	0.19	4	1	0.18

DPP dose per pulse, *PRF* pulse repetition frequency, *ADR* average dose rate

left thigh, where the tumoral lesion was located in the case of tumor bearing mice. This choice allows the precise positioning of the electron beam on the tumoral lesion and the maximum spare of surrounding tissues, thanks to the homogeneous irradiated area (7 mm diameter). As shown in Fig. 1b, the animal was fixed by its teeth on a 3D printed support perpendicular to the applicator, so that the positioning of each animal would be reproducible.

The dosimetric characterization of our beams was carried out using the fD detector [25] and different dosimeter and measurement methods, developed at CPFR and/or provided by other centers [26–34]. An extended description can be found in the supplementary materials (see Additional file 1 [25–34]).

In vivo xenograft melanoma tumor model (pilot study)

B16-F10 murine melanoma cells were cultured in standard conditions according to ATCC protocol [35]. C57BL/6 were anesthetized using volatile isoflurane (induction: 2.5%, maintenance: 1.5%; flow 1 l/min), and the left leg was depilated at the thigh level with shaving cream. A sterile 1-mL syringe fitted with a 26G needle was used to slowly inject a cell suspension (2×10^5 B16-F10 cells in 50 μL of phosphate-buffered saline) intradermally into the leg at an approximately 10° angle relative to the skin surface. After the procedure, animals were allowed to recover in their cages.

3D-Ultrasound measurement of tumor volume

Tumor volumes were measured at several time points along the study by ultrasound using a Vevo 3100 system (FUJIFILM VisualSonics Inc.) as described in the supplementary materials (see Additional file 1). 3D – mode scans (70–150-μm intervals) were imported into the VevoLab software (FUJIFILM VisualSonics Inc.), where the melanoma tumors were identified and semi-automatically marked in the cross-sectional 2D images. Tumor volumes were calculated using the volumetric analysis tool in VevoLab, based on multiple outlined tumor perimeters.

Blood collection and systemic analyses

Blood samples were collected from the tail vein after a 6-h fast to measure glycemia and plasma protein levels, both at baseline (day 0) and at multiple timepoints throughout the experimental procedure. Glucose levels were measured using a OneTouch glucometer (LifeScan). For plasma collection, blood was drawn into EDTA-coated tubes and centrifuged in a refrigerated microcentrifuge ($2000\times g$, 10 min, 4 °C). The plasma fraction was then stored at − 80 °C until analysis. Plasma leptin levels were measured using a Quantikine ELISA Kit (#MOB00B, R&D Systems). Plasma levels of TNFα, IL-6, ghrelin, and insulin were quantified using the Milliplex Extended Hormone Panel (#MMHE-44K, Merck). Both assays were performed following the manufacturer's protocol.

RNA and protein extraction and analysis from mouse tissues

Homogenization of frozen mice tissues (10–25 mg) for RNA and protein isolation was performed with a Qiagen TissueLyser II in 700 μL of TRIzol reagent (#15,596–018, Thermo Fisher Scientific) or 300 μL lysis buffer (50 mM TRIS–HCl, pH 7.4, 150 mM NaCl, 10 mM EDTA, 1% v/v Triton X-100, 10% v/v glycerol) supplemented with protease and phosphatase inhibitors (1:100, #P2850, #P5726, #P8340, Sigma Aldrich), using stainless steel beads at 30 Hz for 5×30 s. mRNA amount of specific genes was evaluated by quantitative PCR as fold increase on TATA Binding Protein gene (TBP) expression. Protein levels of phosphorylated and total S6 ribosomal protein, AKT, and STAT3 were quantified by Western blot analysis and normalized for GAPDH expression. Detailed procedures and reagents employed are available in the supplementary materials (see Additional file 1).

Transcriptomic analysis

Total RNA was assessed for quantity and quality (RIN ≥ 7.5) prior to library preparation. Ribosomal RNA was depleted, and strand-specific libraries were prepared, individually indexed, and pooled for paired-end sequencing on an Illumina NovaSeq X Plus platform. Sequencing reads were processed using the in-house RiDE pipeline

[36], developed at CRS4, which includes alignment, quantification, and quality control steps. Differential expression analysis was performed using DESeq2 [37], followed by functional enrichment analysis with DAVID [38]. Full details of the RNA-seq and bioinformatics analyses are provided in the supplementary materials (see Additional file 1 [36–42]). RNA-seq datasets are available under accession number GSE307570 in the Gene Expression Omnibus (NCBI) [43].

Light microscopy

Dorsal skin samples from the irradiated area of the left hindlimb were processed for histological analysis as described by Castorina et al. [44]. Epidermal and dermal thickness were assessed on hematoxylin and eosin (H&E)-stained sections, while macrophage infiltration was evaluated by immunohistochemistry for CD68. Tissue sections were examined under a light microscope (Zeiss Axioskop 40; Carl Zeiss GmbH), and digital images were acquired using a Zeiss Axiocam 503 color camera. Additional details are provided in the supplementary materials (see Additional file 1 [44]).

Semithin-sections light microscopy and transmission electron microscopy

Murine skin and muscle samples, approximately 1 mm^2 in size, were fixed in 2.5% gluteraldeide and processed for subsequent microscopy analysis as extensively described in the supplementary materials (see Additional file 1). Semithin (800 nm) and ultrathin sections (~ 80 nm) were obtained from resin-embedded tissues. Semithin sections were stained with 1% toluidine blue and 1% sodium tetraborate and imaged using a NanoZoomer-SQ digital slide scanner (Hamamatsu Photonics) for high-resolution light microscopy analysis. Ultrathin sections were collected on copper grids and counterstained with Uranyless and lead citrate. Transmission Electron Microscopy (TEM) imaging was performed with a JEOL JAM-1400 Flash microscope (120 kV), and morphometric analysis of myofibril thickness at the M-line and Z-line was conducted using JEOL SightX Viewer 2.1 software.

Statistical analysis

Graphical representation and statistical analyses were performed using GraphPad Prism. Data are presented as mean ± SEM. Normality was assessed using the Shapiro–Wilk test, and homogeneity of variances using the Brown–Forsythe test. Depending on the experimental design, statistical comparisons were conducted using either one-way ANOVA (or its non-parametric equivalent, the Kruskal–Wallis test) or two-way repeated measures ANOVA with Geisser–Greenhouse correction. When assumptions for repeated measures ANOVA were violated or data were unbalanced, a mixed-effects model was applied. Where appropriate, multiple comparisons were adjusted using Tukey's post hoc test. Survival analyses were performed using Kaplan–Meier survival curves, and group comparisons were assessed with the log-rank test for trend. Correlation analyses were carried out using Pearson's correlation coefficient (r) to evaluate the strength and direction of linear relationships between variables, with associated p values reported for statistical significance. All statistical tests were two-tailed, and a p-value < 0.05 was considered statistically significant.

Results

Comparable tumor control of FLASH- and CONV-RT in a murine model of melanoma

Mice were intradermally injected with melanoma cells into the proximal region of the left hind limb, at the level of the quadriceps muscle (day 0). Three days post-injection, tumor development was confirmed by ultrasound imaging in 100% of animals (Fig. 1a, d). Animals were then randomly assigned to one of three groups to be untreated—controls (CNT), treated with FLASH- or CONV-RT at day 5 post-injection. Between days 11 and 17 post-injection, CNT mice reached humane endpoints due to tumor volumes exceeding 1 cm^3 and were euthanized. In contrast, irradiated mice exhibited delayed tumor progression and prolonged survival, with greater efficacy observed at the higher radiation dose (Fig. 1c–e) for both modalities. Given the superior tumor control achieved with 33.3 Gy, we focused subsequent analyses on this experimental condition, also considering that we need to maximize the potential FLASH effect, which has been reported to be more pronounced at high doses per fraction [16, 45, 46].

CNT, FLASH-, and CONV-treated mice did not differ significantly in BW trajectories (Fig. 1g). In the CNT not irradiated mice, in which tumor size was rapidly reaching the humane endpoint, food intake decreased dramatically over time compared to the treated groups (Fig. 1g), while water intake increased. No notable differences were observed in circulating levels of glucose, insulin, ghrelin, or the inflammatory markers IL-6 and TNFα (Additional file 2: Fig. S2). Interestingly, macroscopic evaluation revealed that the healthy skin surrounding the tumor lesion appeared better preserved in FLASH-RT mice compared to those receiving CONV-RT (Fig. 1f).

Overall, this pilot study supports the iso-effective tumor control achieved by both RT modalities in a dose-dependent manner, while suggesting a potential protective effect of FLASH irradiation on adjacent healthy tissues.

FLASH-RT minimizes damage and transcriptional perturbations in skin

Given the reduced degree of skin damage observed in the peritumoral area of FLASH-treated mice, we sought to further investigate this sparing effect in a controlled setting using naïve, tumor-free animals (experimental design in Fig. 2a). 33.3 Gy dose was selected to assess the impact of RT on normal tissue. To more precisely evaluate radiation-induced skin toxicity, we developed a custom scoring system by integrating and refining existing methodologies [5, 47] to improve the resolution and consistency of damage assessment (Fig. 2b). Details of the procedure are provided in the supplementary materials (see Additional file 1 [5, 47]). Using this approach, we found that CONV-RT mice displayed significantly higher skin damage scores, particularly at early time points, compared to the FLASH-RT group (treatment effect $p < 0.01$, Fig. 2c). These findings support a tissue sparing effect of FLASH-RT on healthy skin.

To further investigate the molecular mechanisms underlying the FLASH effect, we performed bulk RNA sequencing (RNA-seq) on skin samples collected from mice in the CNT, FLASH-, and CONV-RT groups (Fig. 3; Additional file 2: Figs. S3, S4; Additional file 3: Tables S3-S6). Both FLASH- and CONV-RT samples segregated distinctly from controls (Fig. 3a, Additional file 2: Fig. S3a), indicating that RT—regardless of dose rate—induces a measurable transcriptomic response. However, the extent of gene expression changes was markedly greater in CONV-treated mice compared to the FLASH-RT group (Fig. 3a). Using a cutoff of FDR-adjusted $p < 0.05$ and $|\text{fold change}| > 1.5$, we identified 2461 differentially expressed genes (DEGs) in the CONV-RT group (1513 upregulated and 948 downregulated) relative to CNT, whereas only 93 DEGs (42 upregulated and 51 downregulated) were detected in FLASH-treated samples (Fig. 3b). Among the common upregulated genes, to note is the presence of Keratin 6B, likely contributing to an over-keratinization of the skin and thickening of the epidermis in response to stress. Interestingly, this gene was the most upregulated, both in terms of fold change and adjusted p-value in CONV-RT (13.89; adj. $p\text{-value} = 1.69 \times 10^{-69}$) and in this group only was associated with other strongly upregulated keratins such as Keratin 6 A, 16, and 17, known to be involved in injury-induced activation and hyperproliferation of keratinocytes [48, 49]. Conversely, Leptin (Lep) and Perilipin 1 (Plin1) were consistently downregulated in both experimental conditions (Fig. 3b), indicating a potential reduction in the presence and function of the intradermal white adipose tissue (WAT) within the murine skin [50, 51].

When gene ontology (GO) analysis was applied to this dataset, 656 enriched biological process (BP) terms were identified among the genes specifically upregulated in the CONV-RT group ($p < 0.05$), while only 6 significantly enriched terms were found in the FLASH-RT group compared to controls. A more stringent threshold for enrichment significance ($p < 0.001$) resulted in the identification of 195 significantly enriched BP terms among the upregulated genes in the CONV-RT group, whereas only 3 BP terms remained significantly enriched in the FLASH-RT group (Fig. 3c, Additional file 2: Fig. S3b), all of which overlapped with those enriched in the CONV-RT group. As expected, pathway analysis performed using the KEGG database reflected a similar scenario, with 81 enriched terms identified in the CONV-RT group and 2 specific of the FLASH-RT group within the upregulated genes ($p < 0.05$) (Additional file 2: Fig. S4a). In CONV-RT, the most prominently enriched processes and pathways were related to inflammation, fibrosis, keratinization, and cell–matrix interactions, as well as cell death and cell proliferation. Importantly, none of these themes were observed in the FLASH samples (Fig. 3c, e; Additional file 2: Figs. S3b, S4a). Of note, the analysis of CONV-RT upregulated genes highlighted a strong enrichment in both innate and adaptive immunity and inflammatory processes and pathways, including pro-inflammatory

(See figure on next page.)

Fig. 3 Transcriptomic analysis of left hindlimb skin from mice subjected to CONV- and FLASH-RT. RNA-seq was performed on skin samples collected from the irradiated region of the left hindlimb 70 days after mice received 33.3 Gy electron irradiation with either CONV-RT or FLASH-RT, as well as from matched non-irradiated CNT, as detailed in the "Methods" section. Differential gene expression analysis among irradiated and CNT groups was conducted using DESeq2. Genes with an absolute fold change (FC) > 1.5 and a false discovery rate (FDR)-adjusted p-value < 0.05 were considered significantly differentially expressed. Sample sizes: $n = 3$ (CNT and CONV) and $n = 4$ (FLASH). **a** Heatmaps showing differentially expressed genes in CONV vs. CNT and FLASH vs. CNT comparisons. Color range reflects the $\log_2$ fold change between the irradiated group and CNT. **b** Venn diagrams representing the number of significantly upregulated and downregulated genes, and the overlap between FLASH- and CONV-RT conditions. **c**–**e** Functional enrichment analysis of Gene Ontology (GO) biological process (BP) terms among upregulated (**c**) and downregulated (**d**) genes in both CONV- and FLASH-RT groups ($p < 0.001$). Bars represent enriched BP terms ranked by decreasing significance (−log10 p-value). Venn diagrams summarize the number of enriched terms identified in each analysis and their overlap. See Additional file 2: Fig. S3a for additional significant terms. The various annotation terms collected in the figure are color-coded according to their broad categories, which are detailed in the table (**e**); this table also includes the percentages of terms belonging to each category across the different comparisons shown

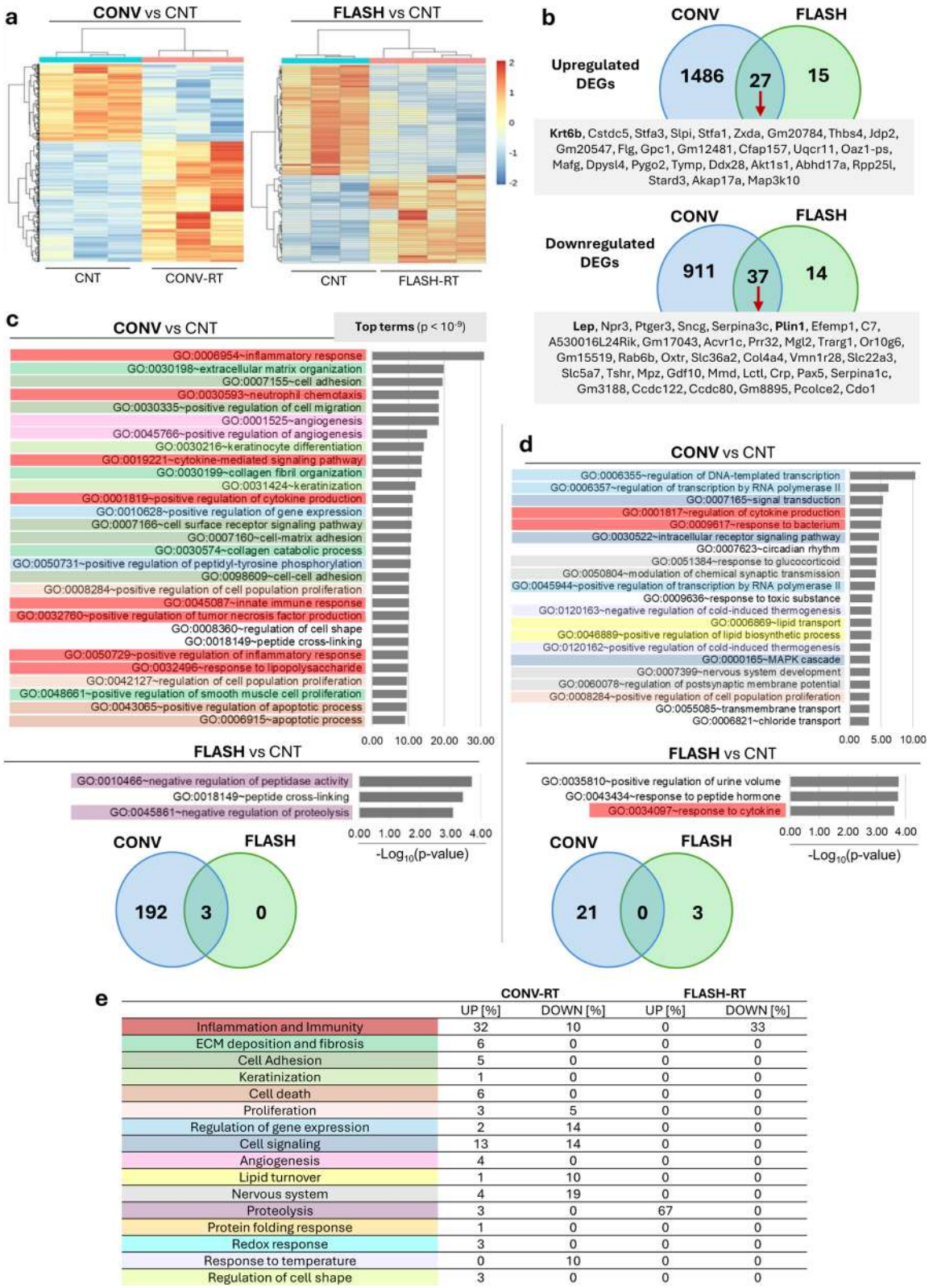

e

	CONV-RT		FLASH-RT	
	UP [%]	DOWN [%]	UP [%]	DOWN [%]
Inflammation and Immunity	32	10	0	33
ECM deposition and fibrosis	6	0	0	0
Cell Adhesion	5	0	0	0
Keratinization	1	0	0	0
Cell death	6	0	0	0
Proliferation	3	5	0	0
Regulation of gene expression	2	14	0	0
Cell signaling	13	14	0	0
Angiogenesis	4	0	0	0
Lipid turnover	1	10	0	0
Nervous system	4	19	0	0
Proteolysis	3	0	67	0
Protein folding response	1	0	0	0
Redox response	3	0	0	0
Response to temperature	0	10	0	0
Regulation of cell shape	3	0	0	0

Fig. 3 (See legend on previous page.)

cytokine signaling (IL-1, IL-6, TNFα, etc.) and leukocyte activity (Fig. 3c, e; Additional file 2: Figs. S3b, S4a).

Among the downregulated genes, applying the same stringent threshold described above ($p < 0.001$), the analysis revealed 21 significantly enriched GO BP terms in CONV-RT mice, compared to only 3 in the FLASH-RT group (Fig. 3d). Similarly, 19 KEGG pathways were enriched in CONV-treated mice and 4 in FLASH-treated mice ($p < 0.05$, Additional file 2: Fig. S4b). Two KEGG pathways, "Regulation of Lipolysis in Adipocytes" and "Hormone Signaling," were enriched in both the CONV-RT and FLASH-RT groups; the intradermal WAT is likely responsible for such feature [52, 53]. In the case of downregulated genes, recurrent themes represented specifically in the CONV-RT enriched BP GO terms were lipid metabolism, transcriptional regulation and neuron related function.

Real-time quantitative PCR was used to validate the differential expression of selected genes identified by RNA-seq (Additional file 2: Fig. S5). Collectively, the data indicate that CONV-RT induces a more extensive transcriptional response in skin tissue compared to FLASH-RT, further supporting the notion of a tissue-sparing effect of FLASH.

Sparing effect of FLASH-RT on skin architecture and histomorphology

To seek independent confirmation of molecular findings, we performed histological analyses. As shown in Fig. 4a, optical microscopy revealed thickening of the skin superficial layer under both irradiation conditions, but significantly more pronounced in the CONV-RT group, reflecting epidermal proliferation and increased collagen deposition. These changes were supported by morphometric analysis (Fig. 4a) and, consistently with a similar response to RT of the different skin compartments, we found a positive correlation between dermal and epidermal thickness (Fig. 4b). TEM data further corroborated these results: in unirradiated controls, TEM showed keratinocyte nuclei arranged in a single layer, consistent with normal squamous epithelium (Fig. 4c). In contrast, irradiated samples exhibited a multilayered epidermis composed of cells with enlarged euchromatic nuclei and hypertrophic nucleoli, indicative of enhanced transcriptional activity particularly pronounced in CONV-treated mice (Fig. 4c). This altered architecture suggests radiation-induced disruption of epidermal homeostasis, likely due to increased turnover and impaired differentiation, especially following CONV-RT exposure. TEM analysis of irradiated samples also revealed enlarged activated dermal fibroblasts with a well-developed endoplasmic reticulum, more prominent in CONV- compared to FLASH-RT. This aspect is associated with the elevated levels of collagen synthesis and secretion observed in irradiated skin (Fig. 4f).

We investigated the inflammatory infiltrate in skin samples and found that, while FLASH-irradiated skin was relatively spared, CONV-irradiated skin showed enhanced staining for the macrophage-specific marker CD68. Morphometry showed that the number of macrophages were significantly higher in dermis of mice irradiated by CONV-RT (Fig. 4d). The number of CD68-positive cells correlated positively with epidermis and dermis thickness (Fig. 4e). In line with these data, TEM analysis revealed the presence of numerous active macrophages in the extracellular matrix of irradiated dermal layer, indicating the presence of an inflammatory response (Fig. 4f). This immune cell infiltration suggests

(See figure on next page.)

Fig. 4 Effect of CONV- and FLASH-RT on histomorphology of healthy skin. Mice were subjected to 33.3 Gy CONV or FLASH-RT to the left hindlimb; matched non-irradiated mice served as CNT. Skin samples were collected 70 days post-RT upon sacrifice. **a** Hematoxylin and eosin (H&E)-stained skin sections. Representative images (left) show epidermal (black line) and dermal (red line) thickness; scale bar, 100 µm. Quantification of epidermal and dermal thickness is shown in the graphs (right). Data are presented as mean ± SEM. Sample sizes: $n = 3$ (CNT and CONV) and $n = 4$ (FLASH), ≥ 20 measurements per sample. Statistical analysis: one-way ANOVA (Epidermal thickness — $F = 15.15$, $p = 0.0029$; Dermal thickness — $F = 11.47$, $p = 0.0062$) followed by Tukey's multiple comparison test. **b** Relationship between epidermal and dermal thickness across all samples: the regression line (solid) illustrates the significant linear association. **c** TEM images of the epidermis. Red arrows: nuclei of epithelial cells, which are arranged in a single layer in CNT and in multiple layers following irradiation (FLASH and CONV); epithelial cells from irradiated skin display euchromatic nuclei. Asterisks: prominent nucleoli, observed exclusively in the CONV-RT group, suggesting higher transcriptional activity. **d** Immunohistochemical staining for CD68. Representative images are shown (left); scale bar: 20 µm. Quantification of CD68-positive area is presented in the graph (right). Data are expressed as mean ± SEM. Sample sizes: $n = 3$ (CNT and CONV) and $n = 4$ (FLASH), ≥ 3 measurements per sample. Statistical analysis: one-way ANOVA ($F = 88.8236.95$, $p = 0.00021$) followed by Tukey's multiple comparison test. **e** Relationship between epidermal (left) or dermal (right) thickness and CD68 positivity across all samples: the regression line (solid) illustrates the significant linear association. **f** TEM analysis of dermal tissue highlighting the inflammatory infiltrate and fibrotic remodeling; scale bar, 5 µm. Insets show magnified views of the boxed regions. Black arrows: infiltrating macrophages within the extracellular matrix; red asterisk in the black squared inset indicate granular cytoplasm with an increased number of high electron-dense lysosomes. Red outlines: fibroblasts of varying size and morphology, reflecting variable degrees of fibrotic response across samples. In CONV-treated mice only, fibroblasts exhibit a highly developed and dilated rough endoplasmic reticulum (RER) containing proteinaceous material (white asterisks in the inset)

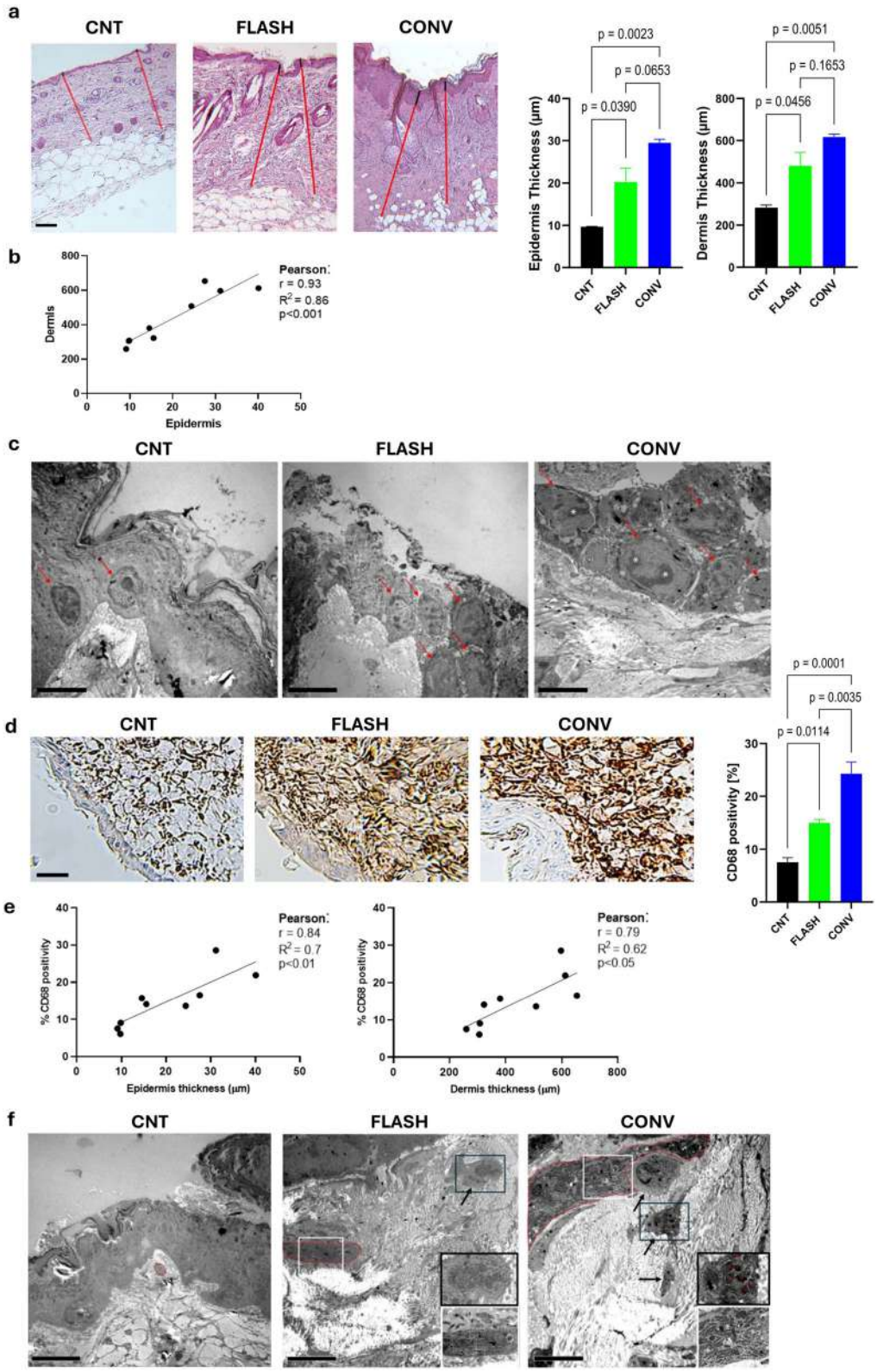

Fig. 4 (See legend on previous page.)

activation of the innate immune response following radiation exposure, contributing to tissue remodeling and repair.

All together, these findings point to a more robust and potentially damaging tissue response in CONV-irradiated skin compared to the relatively spared profile observed with FLASH-RT: major signatures of this damage include fibrosis and inflammation.

CONV-RT, but not FLASH-RT, impacts vital parameters and circulating metabolic and inflammatory markers

We next extended our analysis to evaluate the general health status of the animals. FLASH-RT and CNT groups exhibited overlapping survival curves with undefined median survival times, whereas three mice in the CONV-RT group were euthanized due to extensive lesions in the irradiated left leg, with one case showing lesion extension to off-target areas such as the posterior back and tail region (Fig. 5a). BW change was not different among the three groups, while both food and water intake were influenced by RT with CONV-treated mice displaying the highest values during the medium-term phase after irradiation (Fig. 5b). Glucose, on the other hand, tended to be lower in CONV- compared to FLASH-treated mice (Fig. 5c).

We also measured circulating markers related to inflammation and the endocrine regulation of energy balance. In CONV-RT mice there was a treatment dependent increase over time for circulating IL-6 ($p < 0.01$, Fig. 5d). We then evaluated appetite-related hormones: leptin was reduced, most markedly in CONV-treated mice (RT fixed effect, $p < 0.05$), whereas ghrelin showed an opposite trend, progressively increasing over time in the CONV-RT group only (RT fixed effect, $p < 0.0001$) (Fig. 5e). This endocrine profile is consistent with a systemic signal promoting enhanced appetite. To capture this imbalance, we calculated an "appetite index" (ghrelin/leptin ratio) as a proxy of perceived starvation. Notably, in the medium/long-term CONV-RT mice displayed higher values compared to CNT and FLASH-RT (Fig. 5e).

Overall, these data suggest that CONV-RT administered to the hindlimb not only affects the irradiated target area but also induces systemic alterations. This effect appears to be markedly reduced — or even absent — when FLASH-RT is used.

Muscle architecture and signaling of the irradiated area are impacted by CONV-, but not FLASH-RT

In the presence of a starvation condition—whether actual or merely perceived—the organism responds by preserving energy and sparing functions or tissues not deemed essential for survival. Among the known responses to starvation, muscle alterations have been described [54, 55]. Analysis of semithin sections from irradiated left quadriceps revealed that muscle fibers in CONV-treated mice exhibited markedly irregular shapes compared to those from CNT or FLASH-treated mice, suggesting more pronounced structural damage upon CONV-RT (Fig. 6a). A progressively fainter staining from CNT to CONV-RT can also be noticed, this being usually associated with tissue damage. TEM analyses revealed the presence of tubular aggregates only in the FLASH-treated muscle fibers. These aggregates are typically associated with stress-related protein misfolding events and are a marker of reversible damage [56] (Fig. 6b). On the other hand, ultrastructural alterations that were either more severe or exclusively present following CONV-RT included nucleolar enlargement within myonuclei, mitochondrial hyperplasia and hypertrophy, widespread sarcomere disorganization, myofibrillar fragmentation, and disruption of the Z-line (Fig. 6b,

(See figure on next page.)

Fig. 5 Overview of systemic effects in irradiated mice. Mice received 33.3 Gy of electron RT to the left hindlimb using either CONV or FLASH delivery. Non-irradiated animals served as CNT. Longitudinal analyses were performed as follows. **a** Kaplan– Meier survival curves. Statistical analysis: Log-rank test for trend. **b** Body weight (expressed as percent change from pre-irradiation baseline), food intake, and water intake. Data are presented as mean ± SEM. Sample sizes: body weight, $n = 5$ (CNT) and $n = 8$ (FLASH and CONV); water and food intake, $n = 2$ and $n = 3$ (FLASH and CONV) cages, with 2–3 weekly measurements per cage. Statistical analysis: matched mixed-effects model (REML) followed by Tukey's multiple comparisons test. Fixed effects: Body-weight change — Time, $F(1.609, 19.13) = 8.134$, $p = 0.0044$; RT, $F(2,18) = 0.7307$, $p = 0.4953$. Food intake — Time, $F(2.249, 21.49) = 0.64$, $p = 0.5547$; RT, $F(2, 86) = 4.21$, $p = 0.0181$. Water intake — Time, $F(2.362, 18.89) = 0.87$, $p = 0.4518$; RT, $F(2, 18) = 12.84$, $p = 0.0003$. **c** Fasting blood glucose and insulin levels. Data are presented as mean ± SEM. Sample sizes: $n = 5$ (CNT) and $n = 8$ (FLASH and CONV). Statistical analysis: matched mixed-effects model (REML) followed by Tukey's multiple comparisons test. Fixed effects: Glucose — Time, $F(2.735, 26.67) = 1.94$, $p = 0.1509$; RT, $F(2, 20) = 2.66$, $p = 0.0945$. Insulin — Time, $F(1.842, 24.86) = 0.67$, $p = 0.5096$; RT, $F(2, 18) = 0.98$, $p = 0.3956$. **d** Circulating pro-inflammatory cytokines. Sample sizes: $n = 4$ (CNT and FLASH) and $n = 3$ (CONV). Statistical analysis: matched mixed-effects model (REML) followed by Tukey's multiple comparisons test. IL-6 — Time, $F(1.941, 13.10) = 5.26$, $p = 0.0217$; RT, $F(2, 8) = 15.66$, $p = 0.0017$. TNFα — Time, $F(2.634, 23.05) = 1.76$, $p = 0.1871$; RT, $F(2, 35) = 1.32$, $p = 0.2802$. **e** Circulating metabolic hormones involved in appetite regulation; a starvation index was calculated as the plasma ghrelin-to-leptin ratio. Sample sizes: $n = 5$ (CNT), $n = 8$ (FLASH) and $n = 7$ (CONV). Statistical analysis: matched mixed-effects model (REML) followed by Tukey's multiple comparisons test. Fixed effects: Ghrelin — Time, $F(2.233, 41.30) = 4.06$, $p = 0.0210$; RT, $F(2, 74) = 14.56$, $p < 0.0001$. Leptin — Time, $F(1.773, 22.60) = 6.09$, $p = 0.0095$; RT, $F(2, 17) = 6.06$, $p = 0.0103$. Ratio — Time, $F(1.328, 22.57) = 5.80$, $p = 0.0174$; RT, $F(2, 68) = 25.44$, $p < 0.0001$. Comparisons between groups: * = CNT vs CONV; § = CNT vs FLASH; ° = FLASH vs CONV

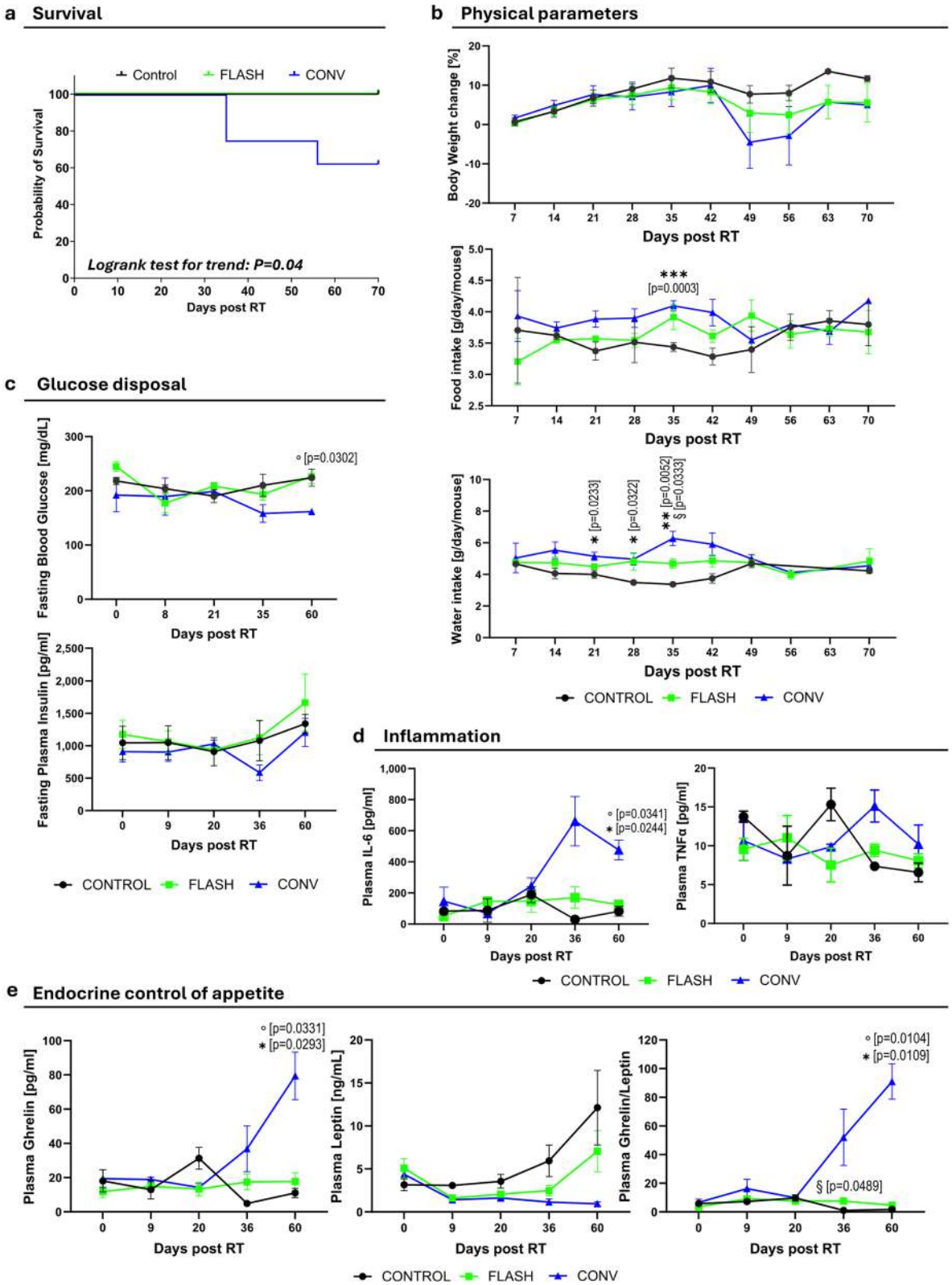

Fig. 5 (See legend on previous page.)

panels 3, 6). Morphometric analysis of TEM images further reinforced these observations. A significant reduction in myofibrillar thickness together with the increase in inter-myofibrils spaces was documented across irradiated groups, with the most evident effects in the CONV-irradiated samples (Fig. 6b, panels 5, 6 and Fig. 6c). Given that myofibrillar density and thickness are critical determinants of contractile function, these data point to a greater degree of functional impairment following CONV irradiation.

Collectively, these findings underscore the differential biological impact of CONV-RT and FLASH-RT on skeletal muscle integrity. While FLASH-RT appears to largely preserve muscle architecture, including the maintenance of myofibril organization and subcellular structure, CONV-RT is associated with extensive architectural disruption, increased inter-myofibrillar spaces, severe damage at both the structural and ultrastructural levels, and stress-induced increase in transcriptional activity and metabolic demand.

Muscle homeostasis is maintained by a finely tuned balance between protein synthesis and protein degradation, primarily regulated by signaling pathways such as mTOR/AKT for anabolic responses and STAT3 for catabolic control. RT can disrupt this balance, triggering compensatory or pathological adaptations. In irradiated mice, we observed a slight, not significant, increase in AKT activation, as measured by the phospho/total AKT ratio (Fig. 6d). Interestingly, total AKT protein levels were significantly upregulated in CONV-treated mice, but not in the FLASH-RT group (Additional file 2: Fig. S6a), suggesting that the induction occurs at the transcriptional and/or translational level. We also detected increased activation of S6, a key downstream effector of the mTOR pathway and central regulator of protein synthesis (Fig. 6d). These findings may reflect a compensatory anabolic response aimed at counteracting prior or ongoing muscle fiber loss, as supported by the structural alterations observed in both histological and ultrastructural analyses. This observation is also consistent with the increased transcriptional activity mentioned above (Fig. 6b). STAT3, a known upstream regulator of the ubiquitin–proteasome system, showed a trend to activation in irradiated muscles, regardless of the RT modality (Fig. 6d), indicating that a catabolic response might also be involved in the muscle loss observed in our model.

Effects of FLASH- and CONV-RT on skeletal muscle molecular signature

Bulk RNA-seq performed on left quadriceps skeletal muscle revealed a transcriptional landscape closely resembling that observed in skin samples, with irradiated muscle transcriptomes clearly segregating from those of controls (Fig. 7a; Additional file 3: Tables S7-S10). As in the skin, the comparison between CONV-RT and CNT mice yielded a markedly higher number of DEGs than the FLASH-RT versus CNT comparison (Fig. 7b). This divergence was clearly reflected in GO and KEGG enrichment analysis (Fig. 7c–e; Additional file 2: Fig. S7). In the CONV group, 93 BPs were significantly enriched among the upregulated DEGs. The most prominently represented broad categories include lipid metabolism and turnover, muscle tissue remodeling, neuronal function, and unfolded protein response, one of the upstream inducers of protein degradation (Fig. 7c, e; Additional file 2: Fig. S7a). Of note, response to starvation was also represented among significantly enriched processes in CONV-RT mice lending support to the abovementioned hypothesis of a perceived status of negative energy balance. Conversely, as for downregulated transcripts, the most significantly enriched BPs were associated with skeletal muscle structure and function (Fig. 7d, e). In the FLASH-RT group upregulated BPs were mainly related to altered inflammatory/immune profile, while no BP

(See figure on next page.)

Fig. 6 Effects of FLASH- and CONV-RT on healthy skeletal muscle ultrastructure and signaling pathways. Mice were subjected to 33.3 Gy CONV or FLASH-RT to the left hindlimb; matched non-irradiated mice served as CNT. Skeletal muscle (*vastus lateralis*) samples were collected 70 days post-RT. **a** Semithin sections stained with toluidine blue. Representative images show irregular fiber morphology and regions of fainter staining, indicative of tissue damage, most pronounced in CONV-treated mice. Scale bar: 200 µm. **b** TEM of ultrathin sections stained with Uranyless and Lead Citrate. Black arrows: intact mitochondria (CNT, panel 4); Black arrowhead: tubular aggregates (FLASH-RT, panel 2); Red arrows: areas of mitochondrial hyperplasia and structural damage (predominantly in CONV-RT, panels 3, 5, 6); Green arrows: multiple nucleoli suggesting transcriptional activation (CONV-RT, panel 6); Black asterisks: enlarged intermyofibrillar sarcoplasmic spaces (more evident in CONV-RT, panels 5, 6). Inset boxes show magnified views. Scale bar: 2 µm. **c** Morphometric analysis of myofibril thickness at the M line in longitudinal skeletal muscle sections. Representative images (left) and quantification (right). Scale bar, 2 µm. Data are presented as mean ± SEM. Sample sizes: $n = 3$; each field contained 30–50 myofibrils, and two fields per sample were analyzed. Statistical analysis: one-way ANOVA ($F = 68.18$, $p < 0.0001$) followed by Tukey's multiple comparison test. **d** Western blot analysis of phosphorylated AKT, S6 ribosomal protein, and STAT3 in muscle lysates. Representative blots (left); red asterisks indicate non-specific bands detected by antibodies against total and phosphorylated S6. Quantification (right) shows the ratio of phosphorylated-to-total protein, calculated after normalization to GAPDH. Data are presented as mean ± SEM. Sample sizes: $n = 3$ (CNT and CONV) and $n = 4$ (FLASH). Statistical analysis: Kruskal–Wallis test ($p_{\text{phospho-AKT/AKT}} = 0.0836$; $p_{\text{phospho-S6/S6}} = 0.0042$; $p_{\text{phospho-STAT3/STAT3}} = 0.0518$), followed by Dunn's multiple comparisons test

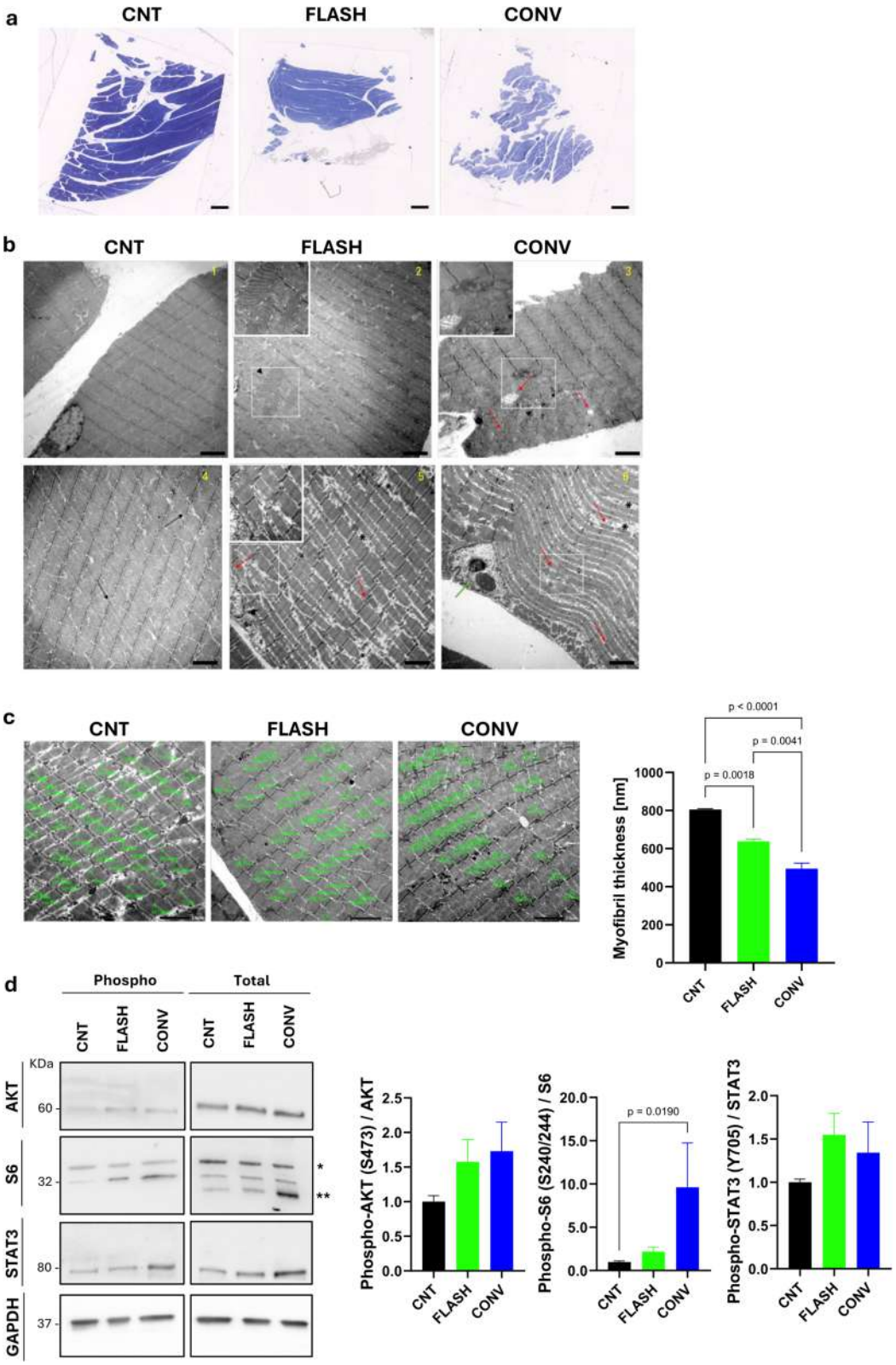

Fig. 6 (See legend on previous page.)

process was enriched among the downregulated genes (Fig. 7c–e).

Discussion

In this study, we adopted a comprehensive preclinical approach to evaluate the dual objectives of tumor control in a murine melanoma model and healthy tissue preservation following electron FLASH-RT. Clinically speaking, FLASH-RT demonstrated iso-efficacy with CONV-RT in reducing melanoma tumor burden, while markedly limiting damage to surrounding healthy tissues—including skin, underlying skeletal muscle, and systemic metabolic and inflammatory parameters.

In line with prior reports, the pilot study herein presented proved the principle that FLASH-RT and CONV-RT achieved iso-effective tumor control in B16-F10 melanoma-bearing mice, with dose-dependent improvements in survival and tumor growth delay. A comparable tumor control between FLASH- and CONV-RT has been reported both with electron beams, as in the murine model of lung cancer [16], and with protons, as in two leg-injected sarcoma models [14]. For the first time, our study demonstrates that the iso-efficacy of CONV and FLASH electron RT also applies to a syngeneic melanoma model. The higher dose (33.3 Gy) resulted in more prolonged tumor growth inhibition, yet complete remission was not observed in any of the experimental groups. This is consistent with other reports, where tumor complete eradication was absent [14]. The known radio-resistance of melanoma [57] therefore offered a stringent model to demonstrate the iso-efficacy of FLASH- relative to CONV-RT. Of note, proton FLASH in combination with immunotherapy has proven effective in increasing survival in mice bearing melanoma [58]. To be considered is that even in the presence of iso-efficacy and comparable sparing effect, proton FLASH-RT faces major challenges, including high costs, the need for large infrastructures, and, consequently, limitations in its widespread clinical translation. In contrast, electron UHDR-RT is more cost-effective, requires substantially less space, and provides a more controlled beam, thereby offering a practical pathway for broader implementation of this technique worldwide.

Interestingly, control mice bearing untreated tumors exhibited a progressive decline in food intake accompanied by an increase in water consumption, particularly near endpoint, when euthanasia was required. BW changes did not parallel food intake as tumor burden (0.7–1 g at sacrifice) contributed substantially (≈4–5%) to total mass. The increased water intake observed has been occasionally reported in cancer-bearing subjects [59, 60], although its etiology remains unclear. One of the most striking differences between CONV and FLASH modalities was observed in healthy skin, where FLASH-RT resulted in markedly reduced acute and chronic damage. Using skin toxicity as primary endpoint, previous studies, employing both electron- and proton-source, report a FLASH effect with substantial sparing of healthy skin, in murine [5–7, 9] as well as in larger animal models such as cats and minipigs [10], with higher doses better highlighting the protective effect. The 33.3 Gy dose used here lies within the effective range reported by Soto [5] (30–40 Gy) and Vozenin [10] (27–40 Gy). In our study, light microscopy revealed marked skin thickening after irradiation, particularly in the CONV group, closely associated with inflammatory infiltration, supporting the established link between epidermal proliferation, fibrosis, and inflammation [61]. Ultrastructural analyses consistently indicated pronounced fibrosis, inflammatory infiltration, and keratinocyte hyperproliferation more pronounced upon CONV-RT. Transcriptomic analyses reinforced these findings: CONV-RT induced thousands of DEGs, particularly in pathways linked to inflammation, fibrosis, keratinization, apoptosis, and extracellular matrix remodeling, whereas FLASH-RT altered only a limited set of transcripts, indicating a more restrained

(See figure on next page.)

Fig. 7 Transcriptomic analysis of left hindlimb muscle from mice subjected to conventional and FLASH RT. RNA sequencing (RNA-seq) was performed on muscle samples (*vastus lateralis)* collected from the irradiated region of the left hindlimb 70 days after mice received 33.3 Gy electron irradiation with either CONV-RT or FLASH-RT as well as from matched non-irradiated CNT, as detailed in the Methods section. Differential gene expression analysis among irradiated and control groups was conducted using DESeq2. Genes with an absolute fold change > 1.5 and a false discovery rate (FDR)-adjusted *p*-value < 0.05 were considered significantly differentially expressed. Sample sizes: $n = 3$ (CNT and CONV) and $n = 4$ (FLASH). **a** Heatmaps showing differentially expressed genes in CONV vs. CNT and FLASH vs. CNT comparisons. Color range reflects the $\log_2$ fold change (FC) between the irradiated group and controls. **b** Venn diagrams representing the number of significantly upregulated and downregulated genes, and the overlap between FLASH- and CONV-RT conditions. **c–e** Functional enrichment analysis of Gene Ontology (GO) biological process (BP) terms among upregulated (**c**) and downregulated (**d**) genes in both CONV- and FLASH-RT groups ($p < 0.05$). Bars represent enriched BP terms ranked by decreasing significance (− log10 *p*-value). Venn diagrams summarize the number of enriched terms identified in each analysis and their overlap. See Additional file 2: Fig S7 for additional significant terms. The various annotation terms collected in the figure are color-coded according to their broad categories, which are detailed in the table (**e**); this table also includes the percentages of terms belonging to each category across the different comparisons shown

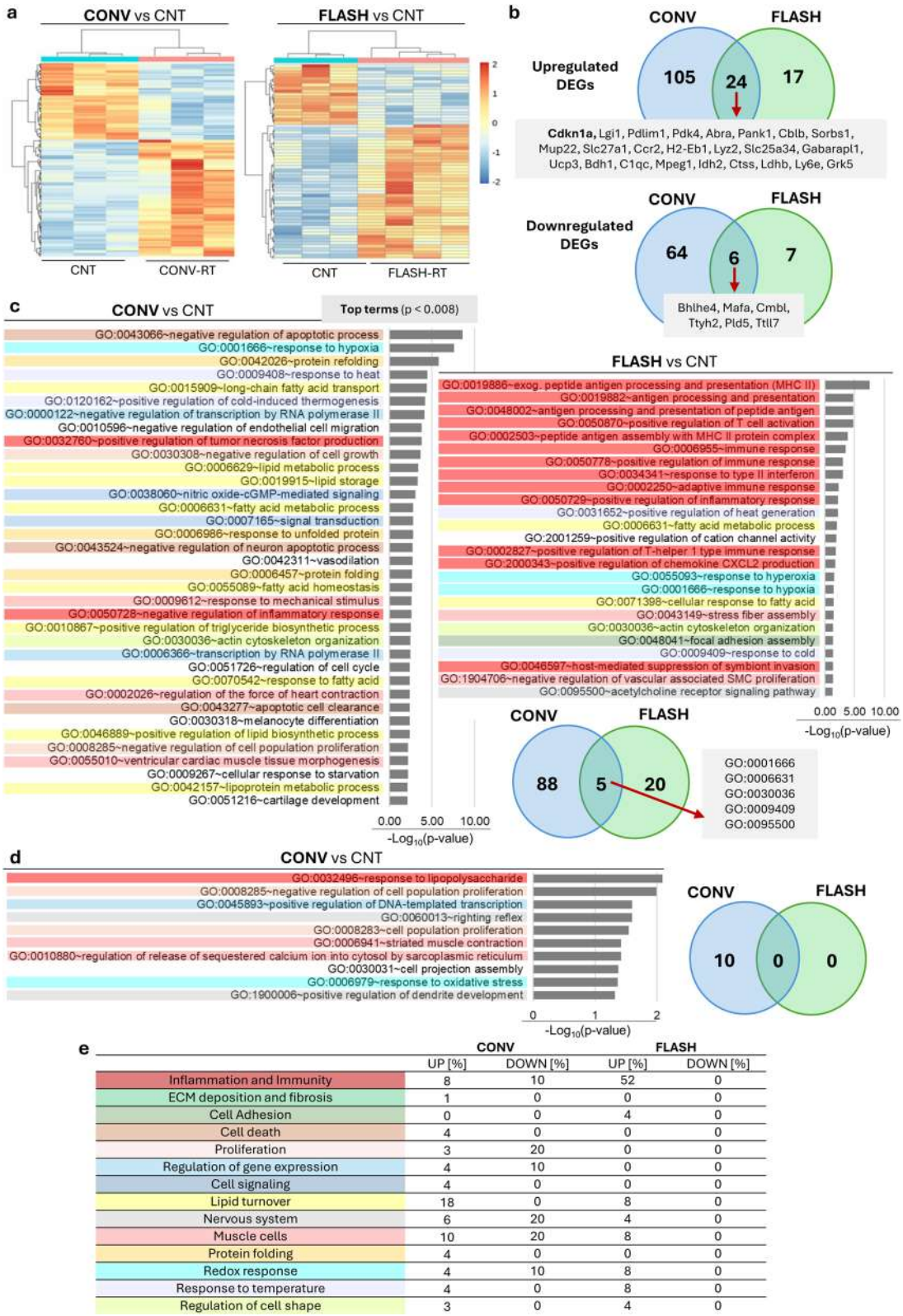

e

	CONV		FLASH	
	UP [%]	DOWN [%]	UP [%]	DOWN [%]
Inflammation and Immunity	8	10	52	0
ECM deposition and fibrosis	1	0	0	0
Cell Adhesion	0	0	4	0
Cell death	4	0	0	0
Proliferation	3	20	0	0
Regulation of gene expression	4	10	0	0
Cell signaling	4	0	0	0
Lipid turnover	18	0	8	0
Nervous system	6	20	4	0
Muscle cells	10	20	8	0
Protein folding	4	0	0	0
Redox response	4	10	8	0
Response to temperature	4	0	8	0
Regulation of cell shape	3	0	4	0

Fig. 7 (See legend on previous page.)

and physiologically contained response. Results partly similar have been reported with proton FLASH-RT: in one study at 30 Gy, skin transcriptomics performed 5 days post-irradiation revealed strong upregulation of apoptotic signaling and keratin pathways in CONV-RT [14]. Interestingly, they reported enrichment of tissue repair pathways uniquely in the FLASH group, whereas we did not observe this feature, likely reflecting both differences in radiation source (protons vs. electrons) and timing of analysis, since our later endpoint (70 days post-irradiation) may have captured a stage when active repair had already subsided. Importantly, our study provides additional value by assessing long-term effects, which may reveal more severe and potentially irreversible consequences. The type and intensity of transcriptional changes herein reported were far greater with CONV-RT, supporting the view that FLASH-RT not only reduces the magnitude of tissue injury, but also prevents the initiation of extensive inflammatory cascades and fibrosis. This is important clinically, as radiation dermatitis is a common and often dose-limiting toxicity in cancer patients [62, 63] and fibrosis may lead to a multitude of pathologies [64].

Beyond the irradiated field, we observed striking differences in systemic physiology. CONV-RT, but not FLASH-RT, triggered widespread systemic alterations, including increased circulating IL-6, reduced leptin, elevated ghrelin, and high ghrelin/leptin ratio in the medium/long-term. This profile is reminiscent of a starvation-like state [65], consistent with decreased glucose levels and increased food intake. Such systemic perturbations can compromise patient well-being during therapy and potentially exacerbate cancer-associated cachexia [66]. In contrast, FLASH-treated animals maintained metabolic and inflammatory profiles similar to controls, suggesting that FLASH irradiation spares not only local tissue integrity but also systemic regulation. These results highlight a critical point: while RT is often considered a localized treatment, its systemic consequences can be profound, and RT-induced cachexia has been previously described [67]. The ability of FLASH to minimize these systemic side effects could represent a transformative advantage, improving patient quality of life and treatment tolerance. During perceived starvation and/or cachexia, the body initiates multiple compensatory mechanisms to preserve the homeostasis of vital functions. Among these, one of the most prominent is skeletal muscle catabolism [68], which serves to release amino acids for gluconeogenesis. Indeed, impairments in muscle structure and altered expression profile were prominent in the muscle of CONV-treated mice. Structural analyses confirmed these deficits, with CONV samples showing disrupted myofibrillar organization and muscle atrophy in line with what previously reported [14]. Additionally, we observed mitochondrial abnormalities and widespread cytoskeletal damage. FLASH-treated muscles, by contrast, largely retained normal architecture, with only reversible tubular aggregates observed. At the molecular level, RNA sequencing again underscored the differential impact of the two modalities. CONV-RT induced widespread transcriptional remodeling, with enrichment of biological processes linked to starvation responses, lipid metabolism, unfolded protein response, and muscle remodeling and neural function. Notably, genes associated with muscle structural integrity were significantly downregulated. In this context, muscle remodeling is inherently linked to adaptations in innervation and neuromuscular junction organization, as structural disorganization of muscle fibers is expected to alter responsiveness to neural input, requiring compensatory adjustments to preserve functional homeostasis [69]. The upregulation of genes related to lipid metabolism and turnover in CONV mice may reflect increased energy demands and the need for membrane repair. This concept is also known as metabolic flexibility [70]. FLASH-RT, on the other hand, produced only minor transcriptional changes, primarily involving immune-related pathways with a substantial preservation of muscle homeostasis and prevention of maladaptive remodeling as that triggered by CONV irradiation.

This study has several limitations that should be acknowledged. First, the number of mice per group in the tumor experiments was limited, which restricts the ability to draw definitive conclusions. In addition, the study focused on melanoma, a relatively rare tumor entity compared to more common skin carcinomas such as squamous cell carcinoma; therefore, the findings may not be directly generalizable in terms of radiotherapy efficacy.

Analyses of normal tissue responses were restricted to skin and skeletal muscle, and other organs at risk were not examined. Moreover, transcriptomic analyses were performed at a single late time point and may therefore have missed early or transient molecular responses. Only male mice were included to reduce biological variability; future studies including both sexes will be important to enhance translational relevance.

Finally, differences in radiation source, fractionation schemes, and treatment timing may influence biological outcomes and limit direct translation to the clinical setting. In particular, the use of a single-fraction high-dose irradiation scheme represents a limitation. Although this approach does not encompass clinically standard multi-fraction regimens, it was intentionally selected based on current evidence indicating that the FLASH effect requires high doses per fraction and is not observed under conventional fractionation. Consequently, the

present findings are most relevant to single-fraction or strongly hypofractionated treatment settings.

Conclusions

In conclusion, this work not only confirms that FLASH-RT achieves tumor control comparable to CONV-RT while preserving normal tissue integrity, systemic homeostasis, and muscle function, but also delineates the pathological trajectory through which CONV-RT leads to its long-term detrimental effects—a pathway that originates with local damage and progressively extends to systemic inflammation and disturbances in perceived nutritional status. This is largely avoided under FLASH conditions. Transcriptomic, histological, and functional analysis collectively demonstrate that FLASH triggers a uniquely restrained biological response, sharply reducing the wave of radiation-induced signaling cascades, systemic stress-like metabolic alterations, and muscle oxidative damage that characterize CONV-RT. This understanding highlights the novelty of FLASH as more than a protective modality: it represents a fundamentally different biological response that could expand the therapeutic window of radiotherapy.

Abbreviations

BPs	Biological processes (GO terms)
BW	Body weight
CNT	Control (non-irradiated)
CONV-RT	Conventional radiotherapy
DEGs	Differentially expressed genes
ECM	Extracellular matrix
FC	Fold-change
FDR	False discovery rate
FLASH-RT	Flash radiotherapy
GO	Gene Ontology
Gy	Gray (absorbed dose unit)
KEGG	Kyoto Encyclopedia of Genes and Genomes
Linac	Linear accelerator
REML	Restricted maximum likelihood
RNA-seq	RNA sequencing
RT	Radiotherapy
TEM	Transmission electron microscopy
UHDR	Ultra-high-dose-rate

Supplementary Information

The online version contains supplementary material available at https://doi.org/10.1186/s12916-026-04724-z.

Additional file 1: Supplementary Methods.

Additional file 2: Supplementary Figures S1-S7. Fig. S1 - Applicator characterization. Fig. S2 - Systemic effects of conventionaland FLASH radiotherapy in the melanoma mouse model. Fig. S3 - Transcriptomic analysis of left hindlimb skin from mice subjected to conventional and FLASH RT, supplementary analyses. Fig. S4 - KEGG pathways enrichment analysis on the irradiation-induced differentially expressed genes the left hindlimb skin. Fig. S5 - Quantitative PCR validation of gene expression changes as identified by RNA-seq in the skin of mice exposed to conventional or FLASH radiotherapy. Fig. S6 - Analysis of signalling pathways regulating muscle homeostasis in response to CONV-RT and FLASH-RT. Fig. S7 - Transcriptomic analysis of left hindlimb muscle from mice subjected to conventional and FLASH RT, supplementary analyses.

Additional file 3: Supplementary Tables S1-S10. Table S1 - Number of mice allocated to each experimental parameter. Table S2 - Details of Probes and Primers for qPCR. Table S3 - Upregulated genes in CONV-RT mice skin compared to CNT. Table S4 - Downregulated genes in CONV-RT mice skin compared to CNT. Table S5 - Upregulated genes in FLASH-RT mice skin compared to CNT. Table S6 - Downregulated genes in FLASH-RT mice skin compared to CNT. Table S7 - Upregulated genes in CONV-RT mice muscle compared to CNT. Table S8 - Downregulated genes in CONV-RT mice muscle compared to CNT. Table S9 - Upregulated genes in FLASH-RT mice muscle compared to CNT. Table S10 - Downregulated genes in FLASH-RT mice muscle compared to CNT.

Additional file 4: Uncropped Western blots from Fig. 6d.

Acknowledgements

The authors acknowledge the support of European Union—Next Generation EU, Mission 4 Component 2 Inv. 1.5, ECS00000017 "Ecosistema dell'innovazione" Tuscany Health Ecosystem—THE project (Spoke 1 'Advanced Radiotherapies and Diagnostics in Oncology'), CUP I53C22000780001. We also acknowledge Fondazione Pisa for funding CPFR with the grant "prog. n.134/2021". A special thanks to Emma Buzzigoli for technical assistance and to Cecilia Ciampi, Sara Ciampi and Gianpietro Chessa for the daily management of animals. The authors used ChatGPT and Google Gemini LLM solely for grammar, spelling, and language editing of this manuscript.

Authors' contributions

AC contributed to the Methodology, Writing (review & editing), and Formal analysis. **AG** contributed to the Methodology **AU** contributed to the Methodology and Writing (review & editing). **CK** contributed to the Methodology, Visualization, Supervision, Writing (review & editing), and Formal analysis. **EG** contributed to the Methodology and Formal analysis. **EMDS** contributed to the Conceptualization, Methodology, Investigation, Visualization, Writing (review & editing) and Data curation. **FDM** contributed to the Conceptualization, Methodology, Funding acquisition, Project administration, Supervision, and Resources. **FF** contributed to the Methodology, Supervision, and Formal analysis. **FP** contributed to the Methodology and Resources. **FR** contributed to the Methodology, Investigation, and Formal analysis. **GA** contributed to the Methodology. **GF** contributed to the Methodology, Investigation, Visualization, Writing (original draft, review & editing), Formal analysis, Validation, and Data curation. **GS** contributed to the Methodology, Investigation, Visualization, Writing (review & editing), Formal analysis, Validation, and Data curation. **JM** contributed to the Methodology, Writing (review & editing) and Formal analysis. **MC1** contributed to the Methodology, Writing (review & editing), and Formal analysis. **MC2** contributed to the Methodology, Supervision and Validation. **MM** contributed to the Conceptualization, Methodology, Investigation, Visualization, Writing (original draft, review & editing), Validation, Funding acquisition, Project administration, Supervision, Resources, Formal analysis, and Data curation. **NG** contributed to the Methodology. **RB** contributed to the Methodology, Writing (review & editing) and Formal analysis. **RC** contributed to the Methodology, Writing (review & editing) and Formal analysis. **RDP** contributed to the Methodology, Visualization, Writing (review & editing), and Formal analysis. **SC1** contributed to the Funding acquisition and Resources. **SC2** contributed to the Funding acquisition and Resources. **SC3** contributed to the Conceptualization, Methodology, Visualization, Supervision, Writing (review & editing), and Validation. **SL** contributed to the Methodology, Investigation, Visualization, Writing (review & editing) and Formal analysis. **TL** contributed to the Methodology, Investigation, Visualization, Writing (review & editing) and Formal analysis. All authors read and approved the final manuscript.

Funding

- European Union—Next Generation EU, Mission 4 Component 2 Inv. 1.5, ECS00000017 'Ecosistema dell'innovazione' Tuscany Health Ecosystem—THE project (Spoke 1 'Advanced Radiotherapies and Diagnostics in Oncology'), CUP I53C22000780001 (MM) and cascading call financed grant RADAR.
- Fondazione Pisa Prog. N. 134/2021.
- PNRR-MAD-2022–12376459, CUP B53C22009530001 (MM)
- MIRO—MInibeam RadiOtherapy Program: INFN CSN5 Call 2024–2026 (MM).
- AIRC—IG 2024 ID-30434 project (MC).

Data availability
RNAseq datasets generated and analysed during the current study are available in the Gene Expression Omnibus repository, under the accession number GSE307570 (https://www.ncbi.nlm.nih.gov/geo/query/acc.cgi?acc=GSE307570). All other data used and analysed during the current study are available from the corresponding author on reasonable request.

Declarations

Ethics approval and consent to participate
All procedures were carried out in accordance with the Helsinki guidelines for animal experimentation and approved under Authorized Protocol 1006/2023-PR, dated November 28, 2023 by the Italian Ministry of Health.

Consent for publication
Not applicable.

Competing interests
The authors declare no competing interests.

Author details
[1]National Research Council, Institute of Clinical Physiology, Pisa, Italy. [2]Centro Pisano Ricerca E Implementazione Clinica Flash Radiotherapy (CPFR@CISUP), Pisa, Italy. [3]Center for Instrument Sharing of the University of Pisa (CISUP), University of Pisa, Pisa, Italy. [4]National Research Council, Institute of Neuroscience, Pisa, Italy. [5]Department of Medicine and Ageing Sciences, "G. d'Annunzio" University of Chieti-Pescara, Chieti, Italy. [6]Department of Medical, Surgical Sciences and Advanced Technologies "G.F. Ingrassia", University of Catania, Catania, Italy. [7]CRS4, Center for Advanced Studies, Research and Development in Sardinia, Pula (CA), Italy. [8]Department of Physics "E. Fermi", University of Pisa, Pisa, Italy. [9]Radiotherapy Unit, Azienda Ospedaliera Universitaria Pisana, Pisa, Italy. [10]Department of Translational Research and New Technologies in Medicine and Surgery, University of Pisa, Pisa, Italy. [11]Department of Experimental and Clinical Medicine, Center of Obesity, Polytechnic University of Marche, Ancona, Italy. [12]Unit of Medical Physics, Pisa University Hospital "Azienda Ospedaliero-Universitaria Pisana", Pisa, Italy. [13]National Institute for Nuclear Physics, Pisa, Italy.

Received: 13 November 2025 Accepted: 16 February 2026
Published online: 26 February 2026

References

1. Gieringer M, Gosepath J, Naim R. Radiotherapy and wound healing: principles, management and prospects (review). Oncol Rep. 2011;26:299–307
2. Bray F, Laversanne M, Sung H, Ferlay J, Siegel RL, Soerjomataram I, et al. Global cancer statistics 2022: GLOBOCAN estimates of incidence and mortality worldwide for 36 cancers in 185 countries. CA Cancer J Clin. 2024;74:229–63.
3. Lao CD, Khushalani NI, Angeles C, Petrella TM. Current State of Adjuvant Therapy for Melanoma: Less Is More, or More Is Better? Am Soc Clin Oncol Edu Book. 2022;738–44.
4. Kim HJ, Kim YH. Molecular frontiers in melanoma: pathogenesis, diagnosis, and therapeutic advances. Int J Mol Sci. 2024;25:2984.
5. Soto LA, Casey KM, Wang J, Blaney A, Manjappa R, Breitkreutz D, et al. FLASH irradiation results in reduced severe skin toxicity compared to conventional-dose-rate irradiation. Radiat Res. 2020;194:618–24.
6. Tavakkoli AD, Clark MA, Kheirollah A, Sloop AM, Soderholm HE, Daniel NJ, et al. Anesthetic oxygen use and sex are critical factors in the FLASH sparing effect. Adv Radiat Oncol. 2024;9:101492.
7. Zhang Q, Gerweck LE, Cascio E, Yang Q, Huang P, Niemierko A, et al. Proton FLASH effects on mouse skin at different oxygen tensions. Phys Med Biol. 2023;68:055010.
8. Sørensen BS, Kanouta E, Ankjærgaard C, Kristensen L, Johansen JG, Sitarz MK, et al. Proton FLASH: impact of dose rate and split dose on acute skin toxicity in a murine model. Int J Radiat Oncol Biol Phys. 2024;120:265–75.
9. Kristensen L, Rohrer S, Hoffmann L, Præstegaard LH, Ankjærgaard C, Andersen CE, et al. Electron vs proton FLASH radiation on murine skin toxicity. Radiother Oncol. 2025;206:110796.
10. Vozenin MC, De Fornel P, Petersson K, Favaudon V, Jaccard M, Germond JF, et al. The Advantage of FLASH Radiotherapy Confirmed in Mini-pig and Cat-cancer Patients. Clin Cancer Res. 2019;25:35–42.
11. Kim MM, Zou W. Ultra-high dose rate FLASH radiation therapy for cancer. Med Phys. 2023;50:58–61.
12. Ni H, Reitman ZJ, Zou W, Akhtar MN, Paul R, Huang M, et al. FLASH radiation reprograms lipid metabolism and macrophage immunity and sensitizes medulloblastoma to CAR-T cell therapy. Nat Cancer. 2025;6:460–73.
13. Cunningham S, McCauley S, Vairamani K, Speth J, Girdhani S, Abel E, et al. FLASH Proton Pencil Beam Scanning Irradiation Minimizes Radiation-Induced Leg Contracture and Skin Toxicity in Mice. Cancers (Basel). 2021;13:1012.
14. Velalopoulou A, Karagounis IV, Cramer GM, Kim MM, Skoufos G, Goia D, et al. FLASH Proton Radiotherapy Spares Normal Epithelial and Mesenchymal Tissues While Preserving Sarcoma Response. Cancer Res. 2021;81:4808–21.
15. Cheng C, Xu L, Jing H, Selvaraj B, Lin H, Pennock M, et al. The Potential and Challenges of Proton FLASH in Head and Neck Cancer Reirradiation. Cancers (Basel). 2024;16:3249.
16. Favaudon V, Caplier L, Monceau V, Pouzoulet F, Sayarath M, Fouillade C, et al. Ultrahigh dose-rate FLASH irradiation increases the differential response between normal and tumor tissue in mice. Sci Transl Med. 2014;6:245ra93.
17. Kim JS, Kim HJ. FLASH radiotherapy: bridging revolutionary mechanisms and clinical frontiers in cancer treatment – a narrative review. Ewha Med J. 2024;47:e54.
18. Di Marco B, Sansevero G, D'Orsi B, De Santis E, Salamone G, Cavalieri A, et al. Unraveling the effects of FLASH and conventional irradiation on retinal pigment epithelial cells: in vitro and in vivo studies. Sci Rep. 2025;15:22938.
19. Klaver YLB, Hoogeman MS, Lu QR, Bradley JD, Choi JI, Ferris MJ, et al. Requirements and Study Design for the Next Proton FLASH Clinical Trials: an International Multidisciplinary Delphi Consensus. Int J Radiat Oncol*Biol*Physics. 2025;123:296–305.
20. Zygogianni A, Kyrgias G, Kouvaris J, Mystakidou K, Gogas H, Kouloulias V. Melanoma: the radiotherapeutic point of view; review of the current literature. Rev Recent Clin Trials. 2011;6:127–33.
21. ClinicalTrials.gov. Clinical trial NCT04986696. https://clinicaltrials.gov/study/NCT04986696.
22. ClinicalTrials.gov. Clinical trial NCT06549439. https://clinicaltrials.gov/study/NCT06549439?cond=NCT06549439&rank=1.
23. Zhou L, Zhu J, Liu Y, Zhou P, Gu Y. Mechanisms of radiation-induced tissue damage and response. MedComm (Beijing). 2024;5:e725.
24. Di Martino F, Del Sarto D, Bass G, Capaccioli S, Celentano M, Coves D, et al. Architecture, flexibility and performance of a special electron linac dedicated to Flash radiotherapy research: electronFlash with a triode gun of the centro pisano flash radiotherapy (CPFR). Front Phys. 2023;11:1268310.
25. Marinelli M, Felici G, Galante F, Gasparini A, Giuliano L, Heinrich S, et al. Design, realization, and characterization of a novel diamond detector prototype for FLASH radiotherapy dosimetry. Med Phys. 2022;49:1902–10.
26. Di Martino F, Del Sarto D, Barone S, Giuseppina Bisogni M, Capaccioli S, Galante F, et al. A new calculation method for the free electron fraction of an ionization chamber in the ultra-high-dose-per-pulse regimen. Phys Med. 2022;103:175–80.
27. Di Martino F, Del Sarto D, Giuseppina Bisogni M, Capaccioli S, Galante F, Gasperini A, et al. A new solution for UHDP and UHDR (Flash) measurements: theory and conceptual design of ALLS chamber. Phys Med. 2022;102:9–18.
28. Di Martino F, Barca P, Barone S, Bortoli E, Borgheresi R, De Stefano S, et al. FLASH Radiotherapy with electrons: issues related to the production, monitoring, and dosimetric characterization of the Beam. Front Phys. 2020;8:570697.
29. Ciarrocchi E, Ravera E, Cavalieri A, Celentano M, Del Sarto D, Di Martino F, et al. Plastic scintillator-based dosimeters for ultra-high dose rate (UHDR) electron radiotherapy. Physica Med. 2024;121:103360.
30. Milluzzo G, De Napoli M, Di Martino F, Amato A, Del Sarto D, D'Oca MC, et al. Comprehensive dosimetric characterization of novel silicon carbide detectors with UHDR electron beams for FLASH radiotherapy. Med Phys. 2024;51:6390–401.
31. Gómez F, Gonzalez-Castaño DM, Fernández NG, Pardo-Montero J, Schüller A, Gasparini A, et al. Development of an ultra-thin parallel plate

ionization chamber for dosimetry in FLASH radiotherapy. Med Phys. 2022;49:4705–14.
32. Cova F, Morrocchi M, Fasoli M, Ciarrocchi E, Pensavalle JH, Gallo S, et al. Stem effect-free (Y,Yb)AG-based detectors for ultra-high dose rate electron beam dosimetry. Sens Actuators A Phys. 2025;390:116539.
33. Romano F, Milluzzo G, Di Martino F, D'Oca MC, Felici G, Galante F, et al. First characterization of novel silicon carbide detectors with ultra-high dose rate electron beams for FLASH radiotherapy. Appl Sci. 2023;13:2986.
34. Del Sarto D, Masturzo L, Cavalieri A, Celentano M, Fuentes T, Gadducci G, et al. A systematic investigation on the response of EBT-XD gafchromic films to varying dose-per-pulse, average dose-rate and instantaneous dose-rate in electron flash beams. Front Phys. 2025;13:1474416.
35. Fidler IJ. Biological behavior of malignant melanoma cells correlated to their survival in vivo. Cancer Res. 1975;35:218–24.
36. Atzeni R, Massidda M, Cuccuru G, Uva P. RIDE – RNA-Seq Differential Expression Pipeline. GitHub https://github.com/solida-core/ride.
37. Love MI, Huber W, Anders S. Moderated estimation of fold change and dispersion for RNA-seq data with DESeq2. Genome Biol. 2014;15:550.
38. Huang DW, Sherman BT, Lempicki RA. Systematic and integrative analysis of large gene lists using DAVID bioinformatics resources. Nat Protoc. 2009;4:44–57.
39. Dobin A, Davis CA, Schlesinger F, Drenkow J, Zaleski C, Jha S, et al. STAR: ultrafast universal RNA-seq aligner. Bioinformatics. 2013;29:15–21.
40. Kent WJ, Sugnet CW, Furey TS, Roskin KM, Pringle TH, Zahler AM, et al. The human genome browser at UCSC. Genome Res. 2002;12:996–1006.
41. Bray NL, Pimentel H, Melsted P, Pachter L. Near-optimal probabilistic RNA-seq quantification. Nat Biotechnol. 2016;34:525–7.
42. Wang L, Wang S, Li W. RSeQC: quality control of RNA-seq experiments. Bioinformatics. 2012;28:2184–5.
43. Furini G, Mota Da Silva E, Usai A, Scabia G, Kusmic C, Rossi F, et al. Localized FLASH Radiotherapy Reduces Long-Term Skin and Muscle Damage While Preserving Systemic Homeostasis; 2025. GEO Database https://www.ncbi.xyz/geo/query/acc.cgi?acc=GSE307570.
44. Castorina S, Barresi V, Luca T, Privitera G, De Geronimo V, Lezoche G, et al. Gastric ghrelin cells in obese patients are hyperactive. Int J Obes. 2021;45:184–94.
45. Montay-Gruel P, Petersson K, Jaccard M, Boivin G, Germond JF, Petit B, et al. Irradiation in a flash: unique sparing of memory in mice after whole brain irradiation with dose rates above 100 Gy/s. Radiother Oncol. 2017;124:365–9.
46. Ilina A, Thomas WS, Cao X, Reed MS, Jarvis K, van der Kogel A, et al. FLASH effect is diminished by daily fractionation of electron RT in mouse skin. Phys Med Biol. 2025;70:235020.
47. Kumar S, Kolozsvary A, Kohl R, Lu M, Brown S, Kim JH. Radiation-induced skin injury in the animal model of scleroderma: implications for post-radiotherapy fibrosis. Radiat Oncol. 2008;3:40.
48. Zhang X, Yin M, Zhang LJ. Keratin 6, 16 and 17-Critical Barrier Alarmin Molecules in Skin Wounds and Psoriasis. Cells. 2019;8:807.
49. Romashin DD, Tolstova TV, Varshaver AM, Kozhin PM, Rusanov AL, Luzgina NG. Keratins 6, 16, and 17 in Health and Disease: A Summary of Recent Findings. Curr Issues Mol Biol. 2024;46:8627–41.
50. Cinti S, Mitchell G, Barbatelli G, Murano I, Ceresi E, Faloia E, et al. Adipocyte death defines macrophage localization and function in adipose tissue of obese mice and humans. J Lipid Res. 2005;46:2347–55.
51. Murano I, Rutkowski JM, Wang QA, Cho YR, Scherer PE, Cinti S. Time course of histomorphological changes in adipose tissue upon acute lipoatrophy. Nutr Metab Cardiovasc Dis. 2013;23:723–31.
52. Li SJ, Wei JQ, Kang YY, Wang RQ, Rong WW, Zhao JJ, et al. Natriuretic peptide receptor-C perturbs mitochondrial respiration in white adipose tissue. J Lipid Res. 2024;65:100623.
53. Lundbäck V, Kulyté A, Dahlman I, Marcus C. Adipose-specific inactivation of thyroid stimulating hormone receptors in mice modifies body weight, temperature and gene expression in adipocytes. Physiol Rep. 2020;8:e14538.
54. Carmeli E, Aizenbud D, Rom O. How Do Skeletal Muscles Die? An Overview Adv Exp Med Biol. 2015;861:99–111.
55. Eston RG, Shephard S, Kreitzman S, Coxon A, Brodie DA, Lamb KL, et al. Effect of very low calorie diet on body composition and exercise response in sedentary women. Eur J Appl Physiol Occup Physiol. 1992;65:452–8.
56. Boncompagni S, Pecorai C, Michelucci A, Pietrangelo L, Protasi F. Long-Term Exercise Reduces Formation of Tubular Aggregates and Promotes Maintenance of Ca2+ Entry Units in Aged Muscle. Fron Physiol. 2021;11:601057.
57. Krayem M, Ghanem GE, Van Gestel D. Recent advances in radiosensitivity determinants in melanoma. Curr Opin Oncol. 2022;34:131–8.
58. Dong YC, Nieves LM, Hsu JC, Kumar A, Bouché M, Krishnan U, et al. Novel combination treatment for melanoma: FLASH radiotherapy and immunotherapy delivered by a radiopaque and radiation responsive hydrogel. Chem Mater. 2023;35:9542–51.
59. Morrison SD. Effect of Growth of a Tumor on the Regulation of Water Intake. JNCI: J Nat Can Inst. 1968;41:1241–8.
60. Morita T, Tei Y, Tsunoda J, Inoue S, Chihara S. Determinants of the sensation of thirst in terminally ill cancer patients. Support Care Cancer. 2001;9:177–86.
61. Dombrowsky AC, Schauer J, Sammer M, Blutke A, Walsh DWM, Schwarz B, et al. Acute Skin Damage and Late Radiation-Induced Fibrosis and Inflammation in Murine Ears after High-Dose Irradiation. Cancers (Basel). 2019;11:727.
62. Borrelli MR, Shen AH, Lee GK, Momeni A, Longaker MT, Wan DC. Radiation-induced skin fibrosis. Ann Plast Surg. 2019;83:S59-64.
63. Rosenthal A, Israilevich R, Moy R. Management of acute radiation dermatitis: a review of the literature and proposal for treatment algorithm. J Am Acad Dermatol. 2019;81:558–67.
64. Lin A, Giuliano CJ, Palladino A, John KM, Abramowicz C, Yuan M Lou, et al. Off-target toxicity is a common mechanism of action of cancer drugs undergoing clinical trials. Sci Transl Med. 2019;11:eaaw8412.
65. Jéquier E. Leptin signaling, adiposity, and energy balance. Ann N Y Acad Sci. 2002;967:379–88.
66. Baracos VE, Martin L, Korc M, Guttridge DC, Fearon KCH. Cancer-associated cachexia. Nat Rev Dis Primers. 2018;4:17105.
67. Shin E, Kang H, Lee H, Lee S, Jeon J, Seong K, et al. Exosomal plasminogen activator inhibitor-1 induces ionizing radiation-adaptive glioblastoma cachexia. Cells. 2022;11:3102.
68. Wang T, Zhou D, Hong Z. Sarcopenia and cachexia: molecular mechanisms and therapeutic interventions. MedComm (Beijing). 2025;6:e70030.
69. Yamaguchi T, Kouzaki K, Sasaki K, Nakazato K. Alterations in neuromuscular junction morphology with ageing and endurance training modulate neuromuscular transmission and myofibre composition. J Physiol. 2025;603:107–25.
70. Smith RL, Soeters MR, Wüst RCI, Houtkooper RH. Metabolic flexibility as an adaptation to energy resources and requirements in health and disease. Endocr Rev. 2018;39:489–517.

Publisher's Note